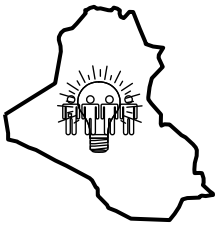

SPONSORED AND PUBLISHED BY
THE IRAQI SOCIETY FOR ALTERNATIVE AND RENEWABLE ENERGY SOURCES AND TECHNIQUES (I.S.A.R.E.S.T.)

EDITORIAL BOARD

ADVISORY BOARD

ORGANIZED BY I.S.A.R.E.S.T.

INVITATION

To all they would like to submit seminars or scientific lectures during the fou rth semester of the **I.S.A.R.E.S.T.** (Octoer, November and Decemer), you are just requested to contact the secretary of the **I.S.A.R.E.S.T.** for date and presentation arrangements of the seminars or lectures. Plesae, do not hesitate to participate in our activities, this chance might be required by young scientists in our country, IRAQ, to develop and grow. You could find us on the post address, emails and mobile below:

Postal:

P. O. Box 55259, Baghdad 12001, IRAQ

Emails:

irq_appl_phys@yahoo.com
editor_ijap@yahoo.com
odayata2001@yahoo.com

Mobile:

00964-1-7901274190

If you would like to meet us, we would so too. You could visit us in Laser Research Unit, University of Technology, Baghdad, IRAQ. You could meet

- **Dr. Walid K. HAMOUDI**
- **Dr. Adawiya J. HAIDER**
- **Dr. Raad A. KHAMIS**
- **Dr. Akram N. MUHAMMAD**

Or you could visit **Dr. Raid A.W. Ismail** at Physics Science and Research Center, Ministry of Science and Technology, Baghdad, IRAQ.

Also, you could visit **Dr. Raad S. Al-Rawi** at Department of Physics, College of Science, Al-Mustansiriya University, Baghdad, IRAQ.

Alaa' B. Kadhim
Bassma H. Hamad*

Physics Science and Research Center, Ministry of Science and Technology, Baghdad, IRAQ,
**Email: basma1980@yahoo.com*

Monte Carlo Simulation of Electronic Kinetics in Gas Discharge

The phenomenon of electrical gas discharge is present in many applications of plasma physics. Calculation of electrons motion tracing in gases are described. The backscattering probability of electrons to the cathode has been estimated for values of E/P_0 ratio from 10 to 200 $V.cm^{-1}.torr^{-1}$ and for emission energies up to the lowest excitation potential. The primary ionization coefficients and drift velocities were evaluated for values of E/P_0 ratio from 20 to 400 $V.cm^{-1}.torr^{-1}$. The equilibrium of swarm with the field was considered in detail. It is shown that for uniform fields, deviations from exponential growth of current with increasing electrode separation occur if the inter-electrode voltage is not at least three times the mean energy of electrons impinging on the anode.

Keywords: *Monte Carlo simulation, Gas discharge, Electronic kinetics*

Received: 19 April 2005, Revised: 12 July 2005, Accepted: 15 July 2005

1. Introduction

Monte Carlo method is used to calculate and evaluate the discharge parameters accurately. This method lends itself well to the study of avalanche growth since the electron densities are usually too small for interactions between charged particles to be important [1]. Thus, the uses of electrons starting from the cathode may be followed quite easily with the assumption of electron- atom collisions only.

Computations are made for electron swarm in neon and the results are used to investigate the velocity of the approximations made in the other methods of calculation mentioned above. Estimations are made of the minimum inter electrode voltages for which the electron swarms can be in equilibrium with the field [2]. Thus setting lower limits on the electrode separations which may be used to measure a mean property of the swarm at any given value of E/P_0. Using the secondary ionization coefficient values to estimate the liberation efficiency of electrons by the incidence of photons or particles on the cathode, it is essential to know the transmission probability (TR) that an electron librated from the cathode will not be scattered back and absorbed. The present work includes calculations to obtain these transmission probabilities over a wide range of E/P_0 values and for emission energies up to lowest excitation potential [3].

2. Monte Carlo Method

Monte Carlo simulation codes that have been used in this work were developed and tested in previous works [2-4]. The set of cross section that was used involves 27 inelastic (excitation) processes, ionization and elastic scattering. Each of these processes associates differential cross section, which is necessary only to establish the angle of scattering. The probability of scattering is determined on the basis of the total cross section.

3. The Problem

For the E/P_0 values considered in this study, the rate at which electrons lose energy by elastic collisions can be neglected. If an electron is ejected from the cathode with energy ε_0 into a uniform field E which is perpendicular to the cathode, then an inelastic collision is supposed to occur, the electron energy at a perpendicular distance x from the cathode may be written as:

$$\varepsilon = \varepsilon_0 + E\,x \qquad (1)$$

where ε_0 is the initial electron energy. We assume that ε_0=0.1eV at x=0 and follow the subsequent motions of electrons.

The values of transmission probability (TR) were calculated by the Monte Carlo method for values of E/P_0 from 10 to 200V.cm^{-1}.$torr^{-1}$ by the Thomson formula:

$$TR=1/[1+\bar{u}/w] \qquad (2)$$

where $\bar{u}$ is the mean emission velocity of electrons from the surface and w is the

equilibrium velocity. Using the values of w determined in the present work, it was found that Eq. (2) estimates the transmission probability (TR) from 0 to 1 using Monte Carlo method. The values of interelectrode voltages V has been evaluated from the equation $\varepsilon=\varepsilon_0+V$, also the electron mobility has been found from equation $\mu=w(E/P_0)^{-1}$ for different values of E/P_0. To calculate the primary ionization coefficient (α/P_0) one can use the Monte Carlo simulation to determine the ionization-excitation electron ratio (R) by the following equation:

$$[\varepsilon+\varepsilon_i+R\varepsilon_o]\ \alpha/P_0 = E/P_0 \qquad (3)$$

where ε_i is the ion energy (17eV) [1], ε_o is the electron energy (21.6eV) [1] and ε is the mean electron energy calculated from Eq. (1).

On the other hand, α can be determined from the following equation:

$$\alpha = (d_2-d_1)^{-1} \ln(n_2/n_1) \qquad (4)$$

where d_1 is the distance between the two electrodes, d_2 is the distance between the electron and cathode, the ratio (n_2/n_1) represents the population inversion in gas and it can be estimated using Monte Carlo method [5].

Computer programs were written in Fortran 77 language which have been sequentially executed. A Pentium 3 personal computer was used to execute these programs.

4. Results and Discussion

The transmission probability of electrons backscattering at different values of E/P_0 ratio as a function of emission energy of electron ε are shown in figure (1). These transmission probabilities (TR) have been computed according to Eq. (2) and they are similar in general form. The values of transmission probability (TR), estimated by Monte Carlo method increase as the emission energy of electrons decreases, which means that the high-energetic electrons cannot be backscattered to cathode under elastic collision conditions. Also, the effect of E/P_0 ratio on the transmission probability (TR) has been investigated. It is seen that the transmission probability TR of backscatter increase as E/P_0 ratio increases, so the Monte Carlo method can be used in the region of high electric field near the cathode. Curve E represents the lowest value of E/P_0 where agreement was good for emission energy below 10eV.

The mean electron energy ε_A impinging on each anode has been determined for different values of E/P_0 ratio.

Viewing Eq. (1), we know that the electrons are liberated from the cathode with very low energies than the inter-electrode voltage (V), as illustrated in figure (2) where ε_A is also plotted as a function of higher values of V for three values of E/P_0. It is seen that the mean energy of electron rises sharply to its final value, say ε_F, for low values of E/P_0 but more gradually for higher values of E/P_0.

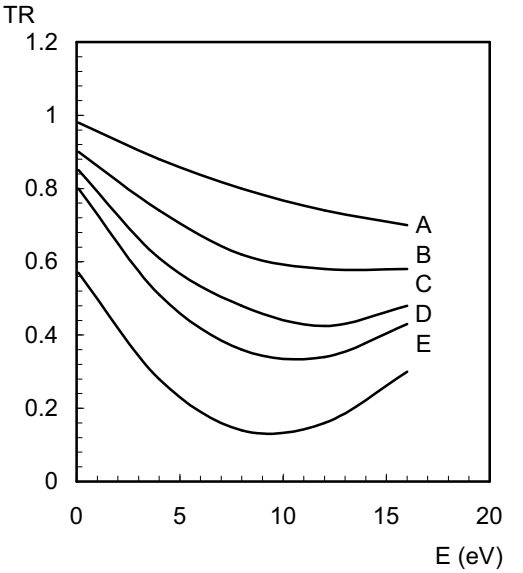

Fig. (1): Transmission probability (TR) versus emission energy (E) for different values of (A) E/P_0 ratio in neon. 200V/cm.torr, (B) 100V/cm.torr, (C) 50V/cm.torr, (D) 30V/cm.torr and (E) 10V/cm.torr

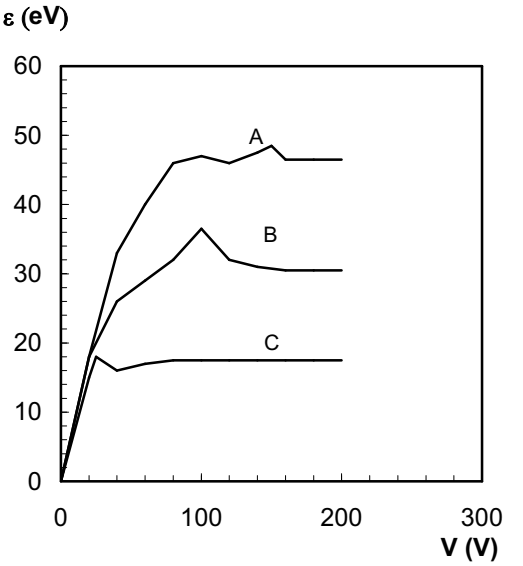

Fig. (2): Mean electron energy at anode as a function of inter electrode voltage for different values of E/P_0 ratio (A) 200V/cm.torr, (B) 100V/cm.torr, (C) 20V/cm.torr

The oscillations in ε_A are related to irregularities across the gap in the rates at which electrons make inelastic collisions and indicate the absence of an equilibrium region.

Figure (3) shows the estimations of primary ionization coefficients (α/P_0), those can be calculated from Eq. (3). The ionization was regarded as an ordinary excitation in which the electron energy was reduced by ε_i. It is seen that

α/P_0 ratio increases with increasing of E/P_0 and reaches the optimum value at E/P_0 of about 250 $V.cm^{-1}.torr^{-1}$.

The estimated electron mobility (μ) has been shown in figure (4) as a function of E/P_0 ratio. It is seen that the electron mobility (μ) decreases as E/P_0 increases.

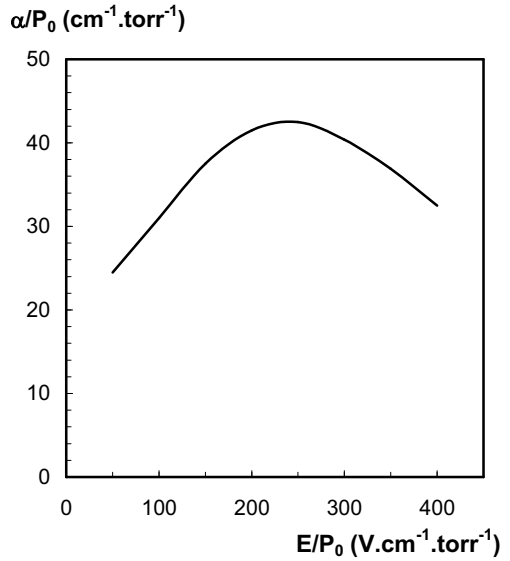

Fig. (3): The primary ionization coefficient (α/P_0) as a function of E/P_0 ratio

5. Conclusions

it has been demonstrated how Monte Carlo calculation can be employed to investigate both electron backscattering to the cathode and avalanche growth. Using the exist data, it is possible to estimate electron energies up to 50eV in neon gas discharge. In order to evaluate the cross section by this method for higher energies, it would e necessary to obtain experimental estimations of the parameter α/P_0 at very high values of the parameter E/P_0. It may be impossible to prove since the enter electrode voltage required for equilibrium between the electron swarm and the field may exceed the breakdown potential.

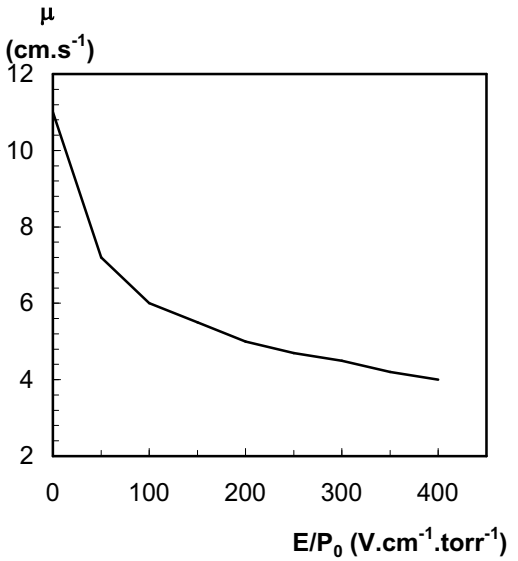

Fig. (4): Electron mobility (μ) as a function of E/P_0 ratio in neon

References

[1] R.W.L. Thomas and W.R.L.Thomas, *J. Phys. B: Atom. Mol. Opt. Phys*., 2 (1969) 562.
[2] J. Bretagne *et al.*, *J. Phys. D: Appl. Phys.*, 19 (1986) 761.
[3] A.V. Phelps, *J. Phy. Ref. Data*, 20 (1991) 557.
[4] T. Holstein, *Phys. Rev.*, 72 (1947) 1213.
[5] J.A. Dahlquist, *Phys. Rev.*, 128 (1962) 225.
[6] S.N. Nahar and J.M. Wadehra, *Phys. Rev.*, A35 (1987) 156.

This article was reviewed at The Korean Advanced Institute for Science and Technology (KAIST), KOREA, Faculty of Management Information, Yamanashi-Gakuin University, JAPAN, and The School of Applied Sciences, University of Technology, Baghdad, IRAQ

September 2005

MAGNETIZED WATERS AND THEIR APPLICATIONS

Let us introduce the following :

- **Application** of a magnetic field of 7000 gauss on flowing water.
- Every cell in human body can be viewed as a small **magnet**.
- Technically, the magnetic field can increase the speed of sedimentation of the suspended particles in water.
- Then it enhances conductivity and ionization/dissociation processes of atoms and molecules.
- Now, you could scale the **pH** of water from **7** to **7.8**.
- ***What does it mean?***
- You can create an alkaline environment in which the **cancer** cells could not survive well.
- Every year, more than **10000000** over world are found to have cancers and **50%** depart (**500** persons/hour).
- How many persons can easily take the magnetized waters **per hour ???.**
- You want to know more?!

IT DESERVES TO ATTEND

In order to interepret all these words and due to the increasing recent interest to the magnetized waters and their medical and environmen tal applications, **I.S.A.R.E.S.T.** arranges to organize an extended seminar on the ***Magnetized Waters and Their Applications*** in September 2005. **Dr. Raad A. Khamis** (School of Applied Sciences, University of Technology) is the lecturer. This is a public invitat ion to attend and benefit of this wonderful progress in technology. Please, contact the secretary of the I.S.A.R.E.S.T. for inquiries and contributions.

Investigation of Amorphous to Crystalline Transition in Glassy $Se_{80}Te_{20}$ and $Se_{70}Te_{20}M_{10}$ (M = Ag, Cd, Sb) Alloys

Neeraj Mehta
Ashok Kumar*

Department of Physics,
Harcourt Butler
Technological Institute
Kanpur – 208 002, India
**Email:*
dr_ashok_kumar@yahoo.com

Calorimetric measurements have been performed in binary $Se_{80}Te_{20}$ and ternary $Se_{70}Te_{20}M_{10}$ (M=Ag, Cd, Sb) alloys to study the effect of metallic additives (Ag, Cd, Sb) on the crystallization kinetics in $Se_{80}Te_{20}$ alloy. Three different non-isothermal methods Kissinger's method, Matusita-Sakka theory and Augis-Bennett approximation method have been used in the present study. Different kinetic parameters such as the activation energy of crystallization (E_C), the order parameter (n), the growth morphology parameter (m), the rate constant (K) and its frequency factor (K_o) have been determined.

The effect of third element on crystallization temperature of binary $Se_{80}Te_{20}$ is explained in terms of Arrhenius dependence of rate constant K(T). The increasing sequence of activation energy of crystallization in ternary $Se_{70}Te_{20}M_{10}$ (M=Ag, Cd, Sb) alloys is explained in terms of their average bond strength.

Keywords: *Chalcogenide glasses, Differential Scanning Calorimetry, Crystallization kinetics*

Received: 12 April 2005, Revised: 12 July 2005, Accepted: 12 July 2005

1. Introduction

Reversible optical information based on the amorphous to crystalline (a-c) transformation of chalcogenide glasses was first studied in the early 1970's [1,2]. A particular "phase change" technique, termed reverse mode recording, records data by quenching amorphous spots in the material with short laser pulses and erases data by crystallizing with long laser pulses. Phase change (PC) recording materials are thus designed so as to have two structural forms 'amorphous' and 'crystalline'.

Since the first observation of rapid rewritable laser-induced a-c transitions in chalcogenide glasses by Ovshinsky [1, 2], many chalcogenide glasses have been studied as potential recording materials [3-14]. These materials are Se- and Te-based alloys because Se-Te alloys have an easy amorphization process. Se-Te alloys have gained much importance as recording materials in PC technique because of their attractive advantages (higher photosensitivity, greater hardness and smaller aging effects) as compared to pure a-Se. However, these alloys are found to have some significant problems for this type of application. The two serious problems are the limited reversibility [15] and low crystallization temperature.

As it is widely accepted that addition of a third element to the binary chalcogenide glasses produces stability in these glasses, the above problems can be removed by adding a third element as chemical modifier. In practice, the laser pulse duration used to write and erase is usually several hundred nano-seconds. It is difficult to erase a written spot in such a time scale, if a-c transformation rate of the recording material is not sufficiently high. Thus, the crystallization behaviour at various temperatures is one of the most important features in developing phase change materials. For this reason, the study of crystallization rate and the factors influencing it are very important for the development of new kinds of erasable PC recording materials. The crystallization kinetics of Se-Te alloys are, therefore, studied by various workers [16-23]

Recently, the effect of Ag, Cd and Sb additives on the glass transition kinetics of glassy $Se_{80}Te_{20}$ alloy is reported by our group [24]. In the present work, three different methods of analysis (as described in next section) have been used to study the effect of these additives on the crystallization kinetics of glassy $Se_{80}Te_{20}$ alloy.

2. Theoretical Basis

The a-c transformation in chalcogenide glasses can be investigated by isothermal and non-isothermal methods. In isothermal method, the sample is brought near to crystallization

temperature very quickly and then any physical quantity, which changes drastically, is measured as a function of time. In non-isothermal method, the sample is heated at a fixed rate and heat evolved is recorded as a function of temperature.

A disadvantage of the isothermal method is the impossibility of reaching a test temperature instantaneously and during the time which system needs to stabilize, no measurements are possible. However measurements can be achieved in a relatively rapid and precise manner by DSC technique, which also allows an immediate observation of the a-c transformation. Various theoretical methods have been suggested to determine activation energy of crystallization from non–isothermal DSC data.

The crystallization kinetics of amorphous alloys have been intensively studied using the classical Johnson-Mehl-Avrami (JMA) theoretical model [25-27] in which the crystallization fraction (α) can be described as a function of time (t) according to the formula:

$$\alpha(t) = 1 - \exp[-(Kt)^n] \quad (1)$$

where n is the Avrami index and K is the rate constant which is given by:

$$K = K_o \exp(-E_c / RT) \quad (2)$$

here E_c is the activation energy of crystallization, R is the universal gas constant and K_o is also a constant.

Based on JMA model, different authors have developed very diverse methods to study a-c transformation of various alloys. Given below is the details of three important and useful methods, which have been used in the present study:

2.1 Kissinger's relation

According to Kissinger [28], the heating rate β, in terms of peak temperature of crystallization T_c, can be expressed as:

$$ln(\beta / T_c^2) = -E_c / R T_c + \text{constant} \quad (3)$$

This equation is used to calculate the activation energy of crystallization by plotting $ln\,\beta / T_c^2$ vs. $10^3 / T_c$ curve.

2.2 Matusita and Sakka Theory

The extent of crystallization (α) at a temperature T is well expressed by the expression:

$$ln(1-\alpha)^{-1} = (C/\beta^n)[(-nE_c)/RT] \quad (4)$$

derived by Matusita and Sakka [29,30] from the classical JMA equation. For constant temperature, this equation can be written as:

$$ln[ln(1-\alpha)^{-1}] = -nln\beta + \text{constant} \quad (5)$$

From this equation, the value of n can be calculated by plotting $ln[ln(1-\alpha)^{-1}]$ vs $ln\beta$ curves at different temperatures.

Further, since the values of α are independent of β at $T=T_c$ [31], so at $T=T_c$, the equation (4) takes the form:

$$ln\,\beta = -E_c/RT_c + \text{constant} \quad (6)$$

This equation is used to calculate the activation energy of crystallization by plotting $ln\beta$ vs. $10^3/T_c$ curve.

2.3 Method of Augis and Bennett

The activation energy of crystallization E_c can also be determined by an approximation method developed by Augis and Bennett [32]. The relation used by them is of the form:

$$ln\beta/T_c = -E_c/RT_c + lnK_o \quad (7)$$

The activation energy of crystallization can be evaluated by this equation using the plots of $ln\beta/T_c$ against $10^3/T_c$.

3. Experiment

Glassy alloys of $Se_{80}Te_{20}$ and $Se_{70}Te_{20}M_{10}$ (M=Ag, Cd, Sb) were prepared by quenching technique. High purity materials (5N pure) were weighed according to their atomic percentages and were sealed in quartz ampoules under the vacuum of 10^{-5} Torr. Each ampoule was kept inside the furnace at an appropriate temperature (where the temperature was raised at a rate of 3-4^{o}C /min.). The ampoules were rocked frequently for 10 hrs at the maximum temperature to make the melt homogeneous. Quenching was done in ice water and the glassy nature of alloys was checked by x-ray diffraction technique.

The glasses, thus prepared, were ground to make fine powder for DSC studies. 10 to 20 mg of each sample was heated at a constant heating rate and the changes in heat flow with respect to an empty pan were measured. Four heating rates (5, 10, 15 and 20^{o}C/ min) were chosen in the present study. For the sake of accuracy, four measurements were conducted for each heating rate and each specimen under identical conditions. Throughout this paper, the experimental data points are taken as the average value of the four supposedly identical measurements. Best-fit methods are used for plotting the experimental data.

Measurements were made under almost identical conditions so that a comparison of kinetic parameters (n, m, K and E_c) could be made in order to understand the effect of changing the additive element (Ag, Cd, Sb) in ternary alloys $Se_{70}Te_{20}M_{10}$.

4. Results and Discussion

Fig.1 shows the typical DSC thermogram for ternary alloy $Se_{70}Te_{20}Cd_{10}$ at different heating rates. Similar thermograms were obtained for other glassy alloys. It is clear from Fig.1 that well defined endothermic and exothermic peaks are observed at glass transition temperature (T_g) and crystallization temperatures (T_c), respectively.

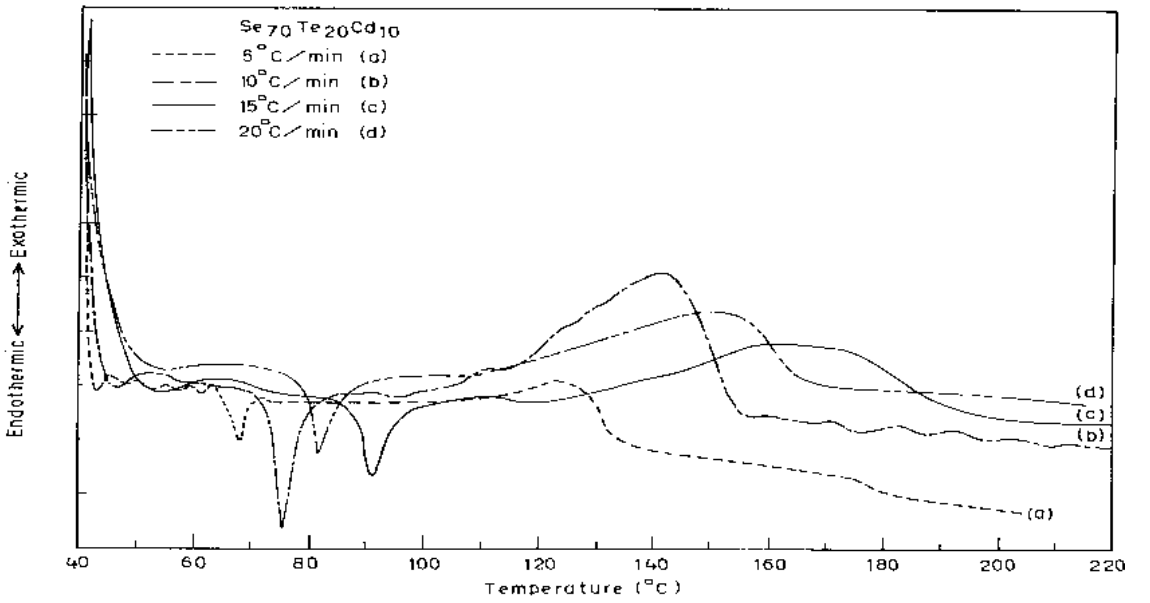

Fig.(1): DSC Thermograms for $Se_{70}Te_{20}Cd_{10}$ alloy at different heating rates

Evaluation of Rate constant and frequency factor

The values of T_c at different heating rates for various glassy alloys are given in Table 1. It is clear from this table that T_c increases on addition of Cd to binary $Se_{80}Te_{20}$ alloy. However, a decrease in T_c is observed in case of Sb and Ag. This can be explained in terms of Arrhenius dependence of $K(T)$. Knowing the values of E_c and lnK_o from Eq. (7), the values of rate constant $K(T)$ have been determined by equation (2). The values of lnK at different temperatures in the crystallization region are given in Table 2.

Table (1) Peak crystallization temperatures of $Se_{80}Te_{20}$ and $Se_{70}Te_{20}M_{10}$ (M=Ag, Cd, Sb) alloys at different heating rates.

Sample	T_c (°C)			
	5 °C/min	10 °C/min	15 °C/min	20 °C/min
$Se_{80}Te_{20}$	118.50	127.40	131.32	135.20
$Se_{70}Te_{20}Ag_{10}$	103.30	109.70	115.30	118.40
$Se_{70}Te_{20}Cd_{10}$	125.60	130.00	136.47	139.23
$Se_{70}Te_{20}Sb_{10}$	87.62	92.00	95.00	100.00

The values of $K(T)$ are increased in the sequence $Se_{70}Te_{20}Cd_{10} < Se_{80}Te_{20} < Se_{70}Te_{20}Ag_{10} < Se_{70}Te_{20}Sb_{10}$. However, the values of T_c are decreased in the sequence $Se_{70}Te_{20}Cd_{10} > Se_{80}Te_{20} > Se_{70}Te_{20}Ag_{10} > Se_{70}Te_{20}Sb_{10}$. This shows that higher the value of $K(T)$, greater the speed of crystallization and hence lower the crystallization temperature.

Table (2) The values of lnK for $Se_{80}Te_{20}$ and $Se_{70}Te_{20}M_{10}$ (M=Ag, Cd, Sb) alloys at different temperatures

Sample	ln K		
	70 °C	80 °C	90 °C
$Se_{80}Te_{20}$	-8.94	-7.87	-6.87
$Se_{70}Te_{20}Ag_{10}$	-7.57	-6.51	-5.51
$Se_{70}Te_{20}Cd_{10}$	-10.49	-9.23	-8.04
$Se_{70}Te_{20}Sb_{10}$	-6.23	-5.02	-3.88
Sample	ln K		
	100 °C	110 °C	120 °C
$Se_{80}Te_{20}$	-5.92	-5.00	-4.16
$Se_{70}Te_{20}Ag_{10}$	-4.56	-3.66	-2.81
$Se_{70}Te_{20}Cd_{10}$	-6.91	-5.84	-4.82
$Se_{70}Te_{20}Sb_{10}$	-2.80	-1.77	0.80

Evaluation of Avrami index n and growth morphology parameter m

The fraction 'α' crystallized at any temperature T is given as $\alpha=A_T/A$, where A is the total area of the exothermic peak between the temperature T_b where the peak begins (i.e. the crystallization starts) and the temperature T_e where the peak ends (i.e. the crystallization is complete). A_T is the partial area of the exothermic peak between the temperatures T_b and T.

Fig. 2 shows the variation of $ln[ln(1-\alpha)^{-1}]$ with $ln\beta$ at three constant temperatures for ternary $Se_{70}Te_{20}Cd_{10}$ alloy. Similar curves were obtained for other glassy alloys. Using Eq. (5), the values of n have been determined from the slopes of these curves at three different temperatures for all the glassy alloys. The values of Avrami index 'n' at three different temperatures are given in Table 3.

Table (3) Values of order parameter n for different alloys

$Se_{80}Te_{20}$		$Se_{70}Te_{20}Ag_{10}$		$Se_{70}Te_{20}Cd_{10}$		$Se_{70}Te_{20}Sb_{10}$	
T (°C)	n	T (°C)	n	T (°C)	n	T (°C)	n
80	2.4	105	3.3	115	1.1	85	1.1
90	2.3	110	3.2	120	0.9	90	1.2
100	2.4	115	3.3	130	1.0	95	1.3

Table (4) Dimensionality factor (growth morphology parameter) m of different alloys

Sample	*m*
$Se_{80}Te_{20}$	2
$Se_{70}Te_{20}Ag_{10}$	3
$Se_{70}Te_{20}Cd_{10}$	1
$Se_{70}Te_{20}Sb_{10}$	1

The numerical factor *m* (growth morphology parameter) of crystallization mechanism representing its dimensionality is given in Table 4. From this table, it is clear that the crystal growth in $Se_{80}Te_{20}$ is two-dimensional. The crystal growth in $Se_{70}Te_{20}Cd_{10}$ and $Se_{70}Te_{20}Sb_{10}$ occurs in one dimension whereas it occurs in three dimensions in $Se_{70}Te_{20}Ag_{10}$.

Evaluation of activation energy of crystallization

The activation energy of crystallization of each alloy has been calculated by Kissinger's relation, Matusita and Sakka theory and method of Augis and Bennett. The plots of $ln(\beta/T_c^2)$ vs. $10^3/T_c$, $ln\beta$ vs. $10^3/T_c$ and $ln(\beta/T_c)$ vs. $10^3/T_c$ for glassy $Se_{80}Te_{20}$ and $Se_{70}Te_{20}M_{10}$ (M=Ag, Cd, Sb) alloys are shown in Figs. 2 to 4, respectively. The values of E_c obtained for all the samples using the above three methods are given in Table 5. Comparison of E_c values of different alloys obtained from equations (3), (6) and (7) shows that the values are in good agreement. This means that one can use any of the three equations to calculate activation energy of crystallization.

It is clear from Table 5 that the activation energy of crystallization indicates the speed of the crystallization. The activation energy of crystallization in ternary alloys have been found to be increase in the sequence $(E_c)_{Ag}<(E_c)_{Sb}<(E_c)_{Cd}$. This sequence can be explained in terms of average heat of atomization for these alloys. The average heat of atomization H_S based on chemical bonding aspects, is defined for an alloy $X_aY_bZ_c$ as a direct measure of cohesive energy i.e., of the average bond strength [33]. H_S can be given as:

$$H_S=[a\,(H_S)_X + b(H_S)_Y + c(H_S)_Z] / (a+b+c) \quad (8)$$

where $(H_S)_X$, $(H_S)_Y$, $(H_S)_Z$ are the heat of atomization of atoms X, Y and Z, respectively. The value of H_S for ternary alloys $Se_{70}Te_{20}M_{10}$ (M=Ag, Cd, Sb) are given in Table 6.

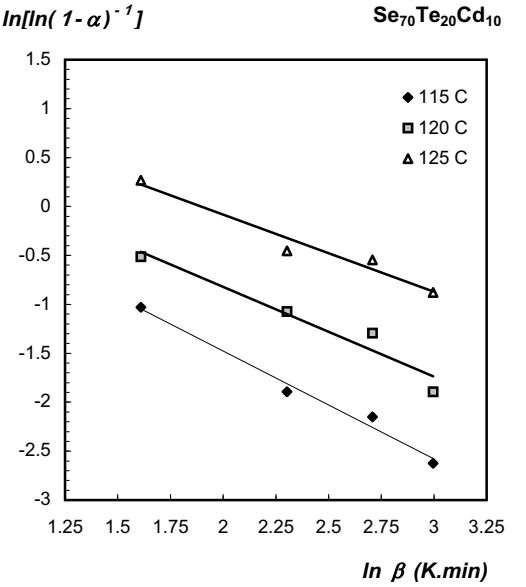

Fig. (2): Plot of $ln[ln(1-\alpha)^{-1}$ vs $ln\beta$ for $Se_{70}Te_{20}Cd_{10}$ alloy

Table (5) Activation energy of crystallization for different alloys

Sample	E_c (eV)		
	Eq. (3)	Eq. (6)	Eq. (7)
$Se_{80}Te_{20}$	1.081	1.149	1.115
$Se_{70}Te_{20}Ag_{10}$	1.074	1.140	1.106
$Se_{70}Te_{20}Cd_{10}$	1.284	1.354	1.319
$Se_{70}Te_{20}Sb_{10}$	1.282	1.294	1.263

Table (6) The average bond strength of ternary $Se_{70}Te_{20}M_{10}$ (M=Ag, Cd, Sb) alloys

Sample	H_S (kJ/mole atoms)
$Se_{70}Te_{20}Ag_{10}$	226.7
$Se_{70}Te_{20}Cd_{10}$	209.5
$Se_{70}Te_{20}Sb_{10}$	224.5

The average bond strength of ternary alloys $Se_{70}Te_{20}M_{10}$ (M=Ag, Cd, Sb) increases in the sequence $(H_S)_{Cd}<(H_S)_{Sb}<(H_S)_{Ag}$. This shows that higher the average bond strength of the ternary alloy, lower is the activation energy and hence the speed of crystallization. The variation of E_c with H_S is shown in Fig. 6.

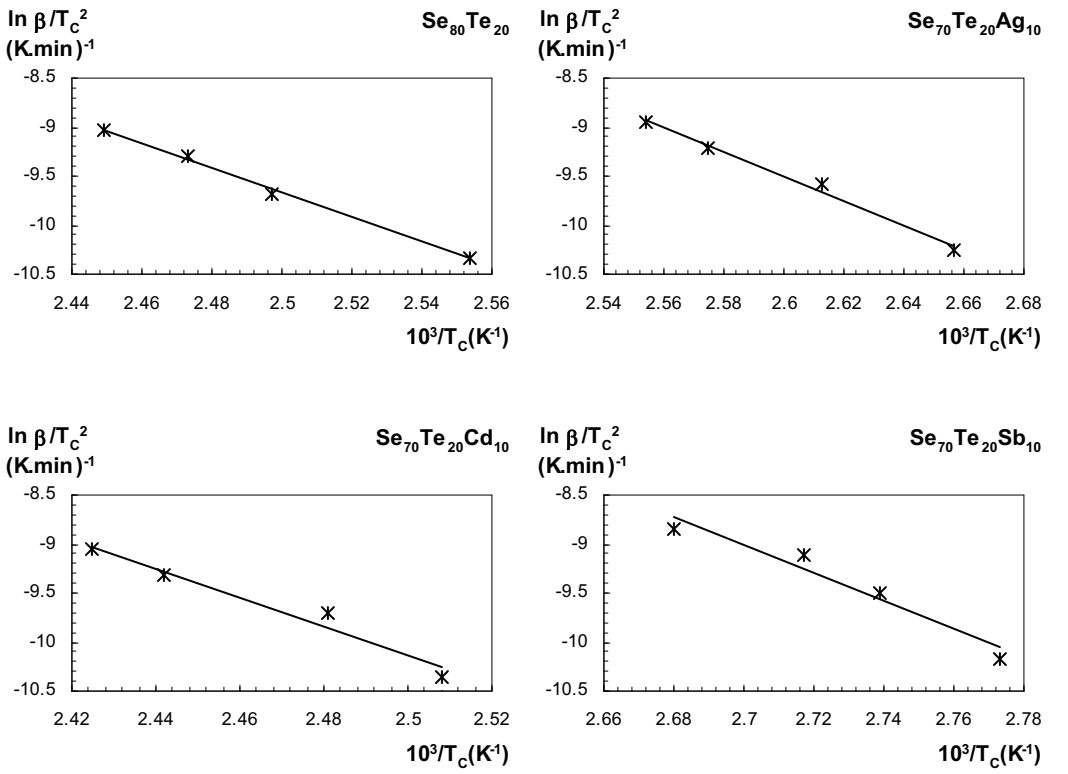

Fig. (3): Plots of $ln\beta/T_c^2$ vs $10^3/T_c$ for different alloys

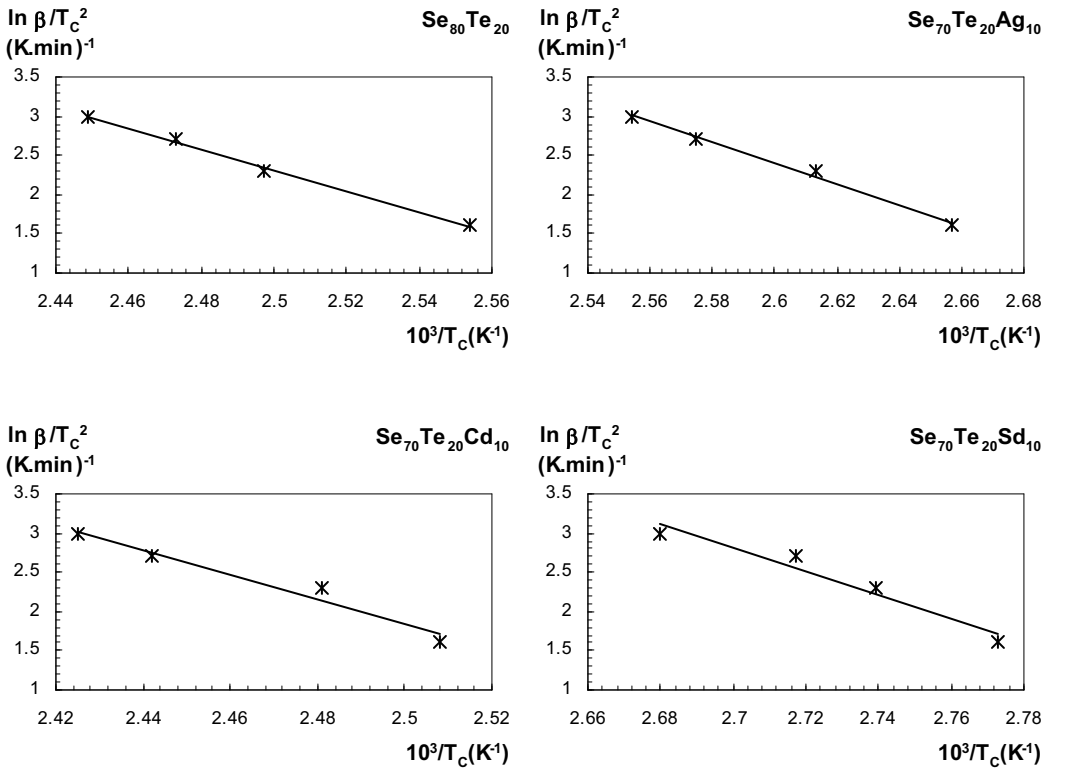

Fig. (4): Plots of $ln\beta$ vs $10^3/T_c$ for different alloys

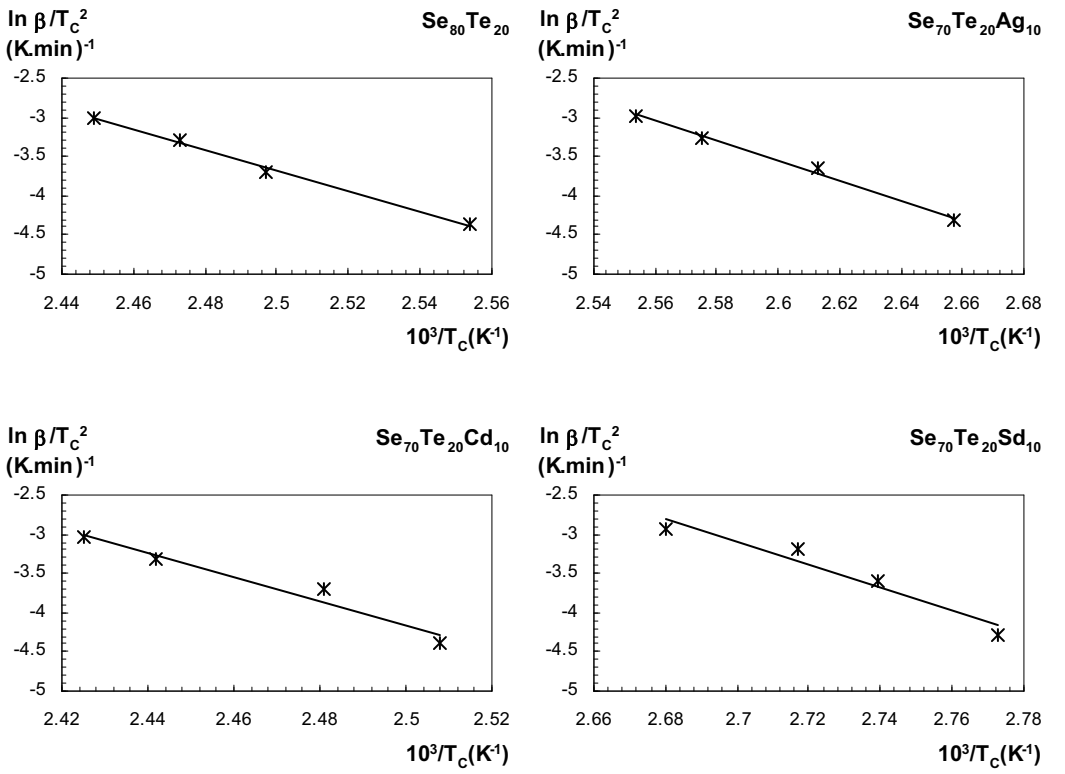

Fig. (5): Plots of $ln\beta/T_c$ vs $10^3/T_c$ for different alloys

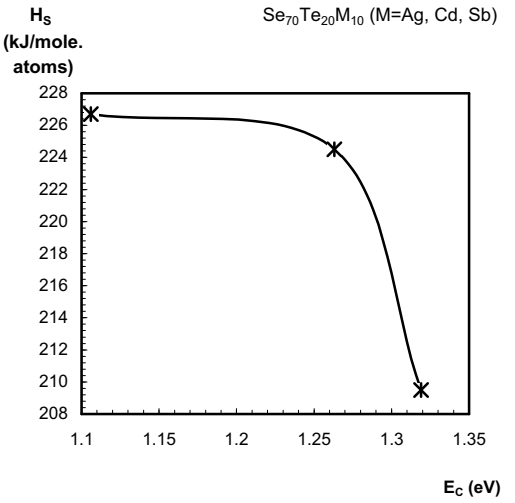

Fig. (6): Plot of E_C vs H_S for ternary $Se_{70}Te_{20}M_{10}$ (M=Ag, Cd, Sb) alloys

5. Conclusions

The effect of some metallic additives (Ag, Cd, Sb) on the crystallization kinetics in glassy $Se_{80}Te_{20}$ alloy has been studied by three different methods under non-isothermal condition. DSC technique has been used in the present study to calculate the activation energy of crystallization. It has been found that E_c values obtained by three different methods are in good agreement with each other.

Different kinetic parameters such as the activation energy of crystallization (E_c), the order parameter (n), the growth morphology parameter (m), the rate constant (K) and its frequency factor (K_o) have been determined.

The effect of third element on crystallization temperature of binary $Se_{80}Te_{20}$ is explained in terms of Arrhenius dependence of rate constant $K(T)$. The present results shows that the speed of crystallization in ternary $Se_{70}Te_{20}M_{10}$ (M=Ag, Cd, Sb) alloys depends on their average bond strength.

References

1. J. Feinleib, J.P. deNeufville, S.C. Moss and S.R. Ovshinsky, *Appl. Phys. Lett.* 18 (1971) 254.
2. J. Feinleib, S.Lsann, S.C. Moss, J.P. deNeufville and S.R. Ovshinsky, *J. Non-Cryst. Solids* 8 (1972).
3. S. Zembutsu, Y. Toyoshima, T. Igo and H. Nagai, *Appl. Opt.* 14 (1975) 3073.
4. S.Y. Suh, D.A. Synder and D.L. Anderson, *Appl. Opt.* 24 (1985) 868.
5. P.F. Carcia, F.D. Kalk, P.e. Bierstedt, A. Ferretti, G.A. Jones and D.G. Swarizfager, *J. Appl. Phys.* 64 (1988) 1715.
6. D.P. Goasin, T. Shimizu, M. Ohmuru, M. Suzuki, T. Bando and S. Okano, *J. Mat. Sci.* 26 (1991) 3271.
7. J. Gonzalez-Hernandez, B. S. chao, D. Strand, S. R. Ovshinsky, D. Pawlik, P. Gasiorowski, *Appl. Phys. Commun.*, 11 (1992) 557.
8. Y. Sripathi, L. K. Malhotra, G. B. Reddy, *Thin Solid Films*, 270 (1995) 60.

9. J. H. Coombs, A. P. J. M. Jongenelis, W. Van Es-Spiekman, B. A. J. Jacobs, *J. Appl. Phys.*, 78 (1995) 4906.
10. J. H. Coombs, A. P. J. M. Jongenelis, W. Van Es-Spiekman, B. A. J. Jacobs, *J. Appl. Phys.*, 78 (1995) 4918.
11. L. Men, F. Jiang, F. Gan, *Mater. Sci. Engin. B*, 47 (1997) 18.
12. N. Yamada, M. Otoba, K. Kawahara, N. Miyagawa, H. Ohta, N. Akahira, T. Matsunaga, *Jpn. J. Appl. Phys.* 37 (1998) 2104.
13. G. F. Zhou, B. A. J. Jacobs, *Jpn. J. Appl. Phys.*, 38 (1999) 1625.
14. V. I. Mikla, I. P. Mikhalko, V. V. Mikla, *Mater. Sci. Engin. B*, 83 (2001) 74.
15. A.W. Smith, *Appl. Opt.* 13 (1974) 795.
16. M. A. Abdel-Rahim, *J. Non-Cryst. Solids*, 241 (1998) 121.
17. A. Singh, J.S.P. Rai and A. Kumar, *Adv. Opt. Electron.*, 9 (1999) 107.
18. N. B. Maharajan, D. Bhandari, N. S. Saxena, D. D. Paudyal, M. Husain, *Phys. Stat. Sol. (a)*, 178, (2000) 663.
19. M. M. Imran, D. Bhandari, N. S. Saxena, *Mater. Sci. Engin. A*, 292 (2000) 56.
20. A. Moharram, A.A. Abu-Sehly, M. Abu El-Oyoun, A.S. Soltan, *Physica B*, 324 (2002) 344.
21. N. B. Maharajan, K. Singh, N. S. Saxena, *Phys. Stat. Sol. (a)*, 195, (2003) 305.
22. N. Mehta, D. Kumar, A. Kumar, *Turk. J. Phys.*, 28 (2004) 397.
23. N. Mehta, M. Zulfequar, A. Kumar, *J. Optoelectron. Adv. Mater.*, 6 (2) (2004) 441.
24. N. Mehta, R. K. Shukla, A. Kumar, *J. Optoelectron. Adv. Mater.*, 6 (4) (2004) 1185
25. W.A. Johnson and R.F. Mehl, *Trans. Am. Inst. Min. (Metal) Engs.* 135 (1939) 416.
26. M. Avrami, *J. Phys. Chem.* 7 (1939) 1103.
27. M. Avrami *J. Phys. Chem.* 8 (1940) 212.
28. H.E. Kissinger, *Anal. Chem.* 29 (1957) 1702.
29. K. Matusita and S.Sakka, *Phys. Chem. Glasses* 20 (1979) 81.
30. K. Matusita and S.Sakka, *Bull. Inst. Chem. Res.* Kyoto Univ. 59 (1981) 159.
31. T. Ozawa, *J. Therm. Anal.* 2 (1970) 301.
32. J.A. Augis and J.E. Bennett, *J. Them. Anal.* 13 (1978) 283.
33. M. Yamaguchi, *Phil. Mag.*, 51 (1985) 651.

This article was reviwed at the Department of Physics, Faculty of Education, University of Hadhramout-Seyoun, YEMEN, and Physics Science and Research Center, Ministry of Science and Technology, IRAQ.

MEETINGS

Optics & Photonics 2005
co-located with the ***SPIE 50th Annual Meeting***
San Diego, California USA 31 July - 4 August 2005 (Exhibition)
Abstracts Due 17 January 2005

Saratov Fall Meeting 2005
26 - 30 September 2005 Saratov, Russia
Sponsored by SPIE Russia Chapter. SPIE will publish proceedings.

Annual Meeting of
The Federation of Analytical Chemistry and Spectroscopy Societies (FACSS 2005)
9 - 13 October 2005 Quebec City, Canada
SPIE is a cooperating organization

CONFERENCES

➢ ***Micro- and Nanoelectronics 2005***
co-located with ***Quantum Informatics 2005***
3 - 7 October 2005 Moscow, Russia
Sponsored by SPIE Russia Chapter. SPIE will publish proceedings.

➢ ***International Conference on Control and Synchronization of Dynamical Systems***
4 - 7 October 2005 Leon, Guanajuato Mexico
SPIE is a cooperating organization

➢ ***Optics East***
23 - 26 October 2005 Boston, MA USA (Exhibition)
Abstracts Due 11 April 2005

➢ ***ETOP 2005 Conference on Education and Training in Optics and Photonics***
23 - 27 October 2005 Marseille, France
Sponsored by SPIE, OSA and ICO

➢ ***The 6th International Young Scientists Conference***
"Optics of High Technology Material Science"
27 - 30 October 2005 Kyiv, Ukraine
Sponsored by SPIE/Ukraine and OSA/Ukraine
Abstracts Due 15 June 2005

➢ ***Optical Technologies for Communications 2005***
28 - 30 November 2005 Ufa, Bashortostan Republic, Russia
Sponsored by SPIE Russia Chapter. SPIE will publish proceedings.

➢ ***International Conference on Optics & Optoelectronics-ICOL 2005***
12 - 15 December 2005 Dehradun, India
SPIE is a cooperating organization

Abdul-Jabbar K. Humady*
Hussain K. Chaiel

Department of Electrical and Electronic Engineering, University of Technology, Baghdad, IRAQ
**Email: abd41_2005@yahoo.com*

Classification of Digital Modulation Using Wavelet Transform

Many methods were presented for classification of digital modulation; these methods either deal with the received (modulated) or the baseband signals. To reduce the classifier complexity, the first type is used. Discrete Fourier Transforms (DFT) or Fast Fourier Transforms (FFT) of the received signal may be used for such purpose. However, the drawback of this method is the time, which required for completing the operation, is proportional to the number of samples used for classification.
In this work, a proposed classifier based on wavelet filters is used instead of the FFT classifier. Computer simulation tests show that the Haar wavelet filter is the most suitable type as compared with other types of wavelet filters. Extra tests show that the wavelet classifier has the same performance but it classify signals with bit rate higher than that of FFT classifier.

Keywords: *Digital Modulation, Wavelet Transform, Digital Communications*

Received: 20 March 2005, Revised: 20 June 2005, Accepted: 20 June 2005

1. Introduction

Modulation classification is the branch of noncooperative communication theory that deals with the task of reporting the modulation type of a received communication signal. Since the problem of automatically classifying the applied modulation type has begun to receive international attention more than 25 years ago, two parties have formed to contribute to this problem [1,2]. The first assumes that an abundant set of apriority information is available, such as carrier frequency, baud rate, received signal and noise power levels, carrier phase, channel characteristics, spectral shaping filter characteristics, etc. In most cases this resulted in a synchronous approach, where a symbol synchronous, sampled, complex valued baseband signal is available to the modulation classification unit [2]. The second group takes into account that apart from the set of possibly used modulation types, there is no such additional information available. The solution of the modulation classification problem there leads in most cases to an asynchronous approach. The proposed features are often generated in the frequency domain using spectral analysis algorithms, to be independent of unknown time domain parameters and the data content.

In recent times, a development of digital electronic circuits leads to progress of high-speed digital signal processing systems. Among these are spectral analysis systems, such as FFT algorithms. However, the complexity of such algorithms is proportional to the number of signal samples (N). Such complexity is in order of $NLog_2N$ arithmetic operations [2,4].

Furthermore, the theory of wavelets has been developed as a new analytic tool and formal framework in both mathematics and computer sciences. Wavelet algorithms such as Discrete Wavelet Transform (DWT) process data at different scales or resolutions. This makes wavelets interesting and useful. The discrete wavelet transforms $C(j,k)$ for the sampled signal f(n) may be defined by [3]:

$$C(j,k) = \sum_{n \in z} f(n)\psi_{j,k}(n) \qquad (1)$$

where z, j and k, are integers and the wavelet function,

$$\psi_{j,k}(n) = 2^{-j/2}\psi(2^{-j}n - k) \qquad (2)$$

Mallat showed that Multiresolution Analysis (MRA) can then be used to obtain the DWT of a discrete signal by iteratively applying low pass and high pass filters, and subsequently down sampling them by two. Figure 1 shows this procedure, where $g[n]$ and $h[n]$ are the high pass and low-pass filters, respectively The frequency bands (in terms of discrete frequencies ω) are also shown in Fig. (1) and the output of the wavelet filters are computed at each level using the following.

$$y_{\text{high}}[k] = \sum_{n} x[n].g[2k-n]$$
$$y_{low}[k] = \sum_{n} x[n].h[2k-n] \quad (3)$$

where

$$h[N-1-n] = (-1)^{n}.g[n] \quad (4)$$

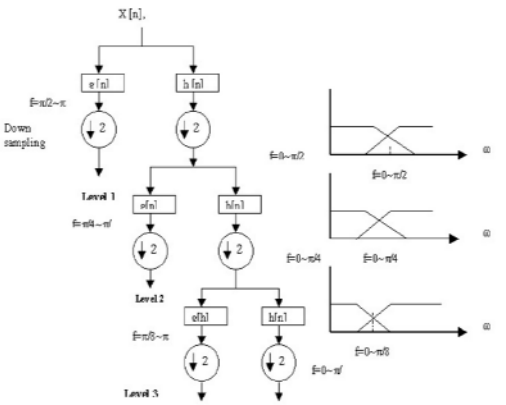

Fig. (1): Computing DWT by MRA

2. The Proposed System

Fig. (2) shows the block diagram of a proposed method used to classify binary digital modulation signals. This system consists of:

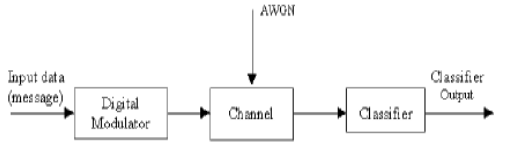

Fig. (2): Block diagram of the proposed system

2.1 Digital Modulator, the digital modulator is used to generate the digital modulated signals. These signals are either ASK, FSK or PSK. The input to the digital modulator is random binary data consisting of one's and zero's. M-ary modulations are not included in this work as a result of detection complexity (multiplication of orthogonal functions).

2.2 Channel, the modulated signal is transmitted through a channel corrupted by zero mean additive white Gaussian noise. The signal to noise ratio may be represented by [4,8]:

$$SNR = \frac{\sum_{i=1}^{N} s_i^{2} / N}{\sum_{i=1}^{N} n_i^{2} / N} \quad (5)$$

$$SNR_{dB} = 10\ Log_{10} SNR \quad (6)$$

where N is number of samples, s_i is signal sample value and n_i is noise sample.

2.3 Classifier, the classifier consists of the following three parts:

i. Sampler: The received signal is sampled with a frequency $f_s \geq 2f_{max}$. In this work, two samples for each bit are taken first and to avoid samples with zero values, four samples for each bit are taken.

ii. Analyzing Algorithm: The second part of classifier is the analyzing algorithm. This is either FFT or DWT algorithm; the samples of modulated signal are used as input data to the (FFT) algorithm. Instead of the FFT algorithm, discrete wavelet transform is used .In this algorithm, two types of wavelet filters is used. The first is low pass filter *h(n)*, while the other is high pass filter *g(n)* the wavelet filters used in these tests are Haar, db2, bior2.2, and coif1 types [2,7].

For two samples/bit, the wavelet analyzer may be described by Fig. (3) the symbol ⬇2 represents down sampling operation. When the sampled signal is sampled with four times the modulated signal, the structure of the wavelet analyzer is shown in Fig. (4).

iii. Decision algorithm: To decide which type of digital modulation analyzed, a decision algorithm is used.

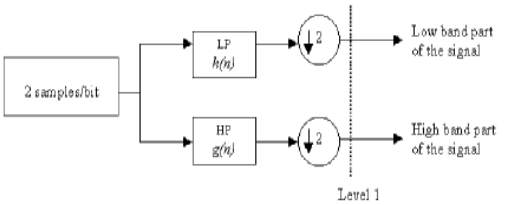

Fig. (3): Structure of 2 samples/bit wavelet analyzer

3. Computer Simulation Tests

Computer simulation tests have been carried out to show the classifiers operation. All tests are done using a PC, P4B computer with a 400MHz processor. The code was developed under MATLAB7 software.

3.1 Two-Samples Signal Classifier with Noiseless Channel

The channel is assumed here to be noiseless. The sampling frequency is twice the received signal frequency, Figures (5) and (6) show two samples PSK signal analysis.

a. Binary digital pulses,
b. PSK waveform,
c. Samples of PSK signal,
d. FFT output,
e. Low pass Haar wavelet filter output, f. High pass Haar wavelet filter output.

Form Figures (5) and (6) one can point the following:

a. For Haar wavelet filter, the output of the FFT and the DWT filters are the same. The output of up sampling operation (multiplexing) for the low pass (Fig. 5e) and high pass (Fig. 5f) is the same as FFT output (Fig. 5d). This result is expected as a result of the same mathematical operation of the two algorithms.

b. For the other wavelet functions, there is a difference between the FFT and DWT filters outputs. Also, the complexity is increased for such wavelet functions as a result of equations 3 and 4.

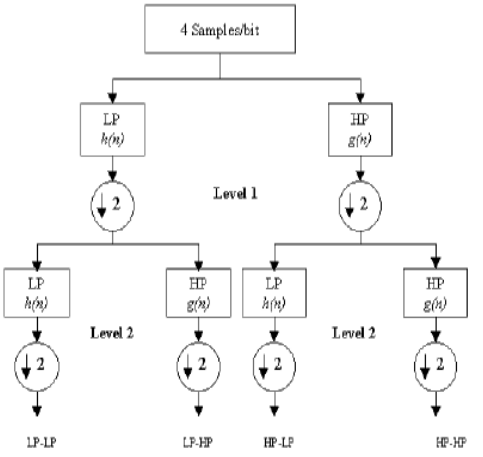

Fig. (4): Structure of 4 samples/bit wavelet analyzer

To choose the most suitable wavelet function for the application of signal classification, consider Fig. 3. Let X_n represents the n^{th} sample of the received signal, $a_0, a_1, \ldots\ldots, a_{N-1}$ are the low pass filter coefficients and $b_0, b_1, \ldots\ldots, b_{N-1}$ are the high pass filter coefficients.

For best classification, the difference between the low pass filter and high pass filter output must be as large as possible [2]. From equation 4, the output of the low pass filter is

$$a_{N-1}x_0 + a_{N-2}x_1 + \ldots\ldots + a_0 x_{N-1} \quad (7)$$

and high pass filter output (equation 3)

$$b_{N-1}x_0 + b_{N-1}x_1 + \ldots\ldots + b_0 x_{N-1} \quad (8)$$

The difference between equations (7) and (8) is

$$(a_{N-1} - b_{N-1})x_0 + (a_{N-2} - b_{N-2})x_1 + \ldots + (a_0 - b_0)x_{N-1} \quad (9)$$

Table (1) difference between LP and HP filters

No	Wavelet family	Equation
1	Haar	$1.4142x_1$
2	db2	$0.3536x_0$-$0.6124x_1$+$1.0606x_2$+$0.6144x_3$
3	bior2.2	$0.1768x_1$+$0.3535x_2$+$1.4143x_3$-$0.3536x_4$-$0.1768x_5$
4	Coif1	-$0.057x_0$+$0.2652x_1$+$0.4677x_2$+$1.2375x_3$-$0.4106x_4$-$0.0884x_5$

The Haar wavelet function coefficients are [2]:

$a_o=0.7071$, $a_1=0.7071$, $b_0=-0.7071$, $b_1=0.7071$

By substituting these values in equation (9)

$$(a_1 - b_1)x_0 + (a_0 - b_0)x_1 = (0.7071 - 0.7071)x_0 + (0.7071 - (-0.7071))x_1 = 1.4142x_1$$

In the same way, the results of the other types of wavelet function with their coefficients are shown in the Table (1). From this table and for Haar type, the difference between the low pass and high pass filters depends on a certain sample value, while for the other wavelet filters, the result depends also on the other successive samples. As a result, the output of the Haar type is larger than the output of other types, so Haar wavelet filters are the most suitable type for such application.

3.2 Four-Samples Signal Classifiers with Noiseless Channel

Sometimes, and due to switching operation and for $f_s=2f_{max}$, the samples may have zero values and to overcome such problems, the number of samples is increased to 4 samples/bit. Figures (7) and (8) show the results of the PSK signal under such test.

a. Low pass-low pass wavelet filter output,
b. Low pass-high pass wavelet filter output,
c. High pass-low pass wavelet filter output,
d. High pass-high pass wavelet filter output.

From Figures (7) and (8), the following points may be concluded:

a) The complexity of DWT is increased as a result of the two levels of filters used, so the final result is taken from four wavelet filters instead of two wavelet filters used for the case of two samples/bit.

b) The FFT algorithm is more complex than DWT and so the time required to complete the classification operation is more than for DWT algorithm.

Let the clock frequency be 50MHz. This means that each operation needs a time of 20ns. For FFT algorithm, there are $N\text{Log}_2N$ operation, and so for N=4 (4samples/bit), the required time is $(4\text{Log}_2 4)\times 20 = 8\times 20 = 160$ ns. While for DWT, there are 2 operations (2 levels), then $2\times 20 = 40$ns. These values indicate that the DWT has the ability of signal classification with bit rate of 25Mbit/sec compared with 6.25Mbit/sec for FFT algorithm (i.e. four times that of FFT).

3.3 Probability of Correct Classification Test

Extra tests have been carried out to show the probability of correct and miss classification of DWT classifier under different values of SNR. Figure 9 shows the flow chart related to the test depends on the similarity of the output of the

wavelet filters with the standard outputs of the different digital modulation types. When the output of the wavelet filter for a certain digital modulated signal is similar to the standard shape, the counter related to the signal under test is increased by one. Therefore, there are four counters, the first for ASK, the second for FSK, the third for PSK and the fourth for any other signal. Related counter is increased by one. Finally the probability of correct classification is calculated by dividing the contents of the counters with the total number of samples (100000).

Tables (2-4) show the result of correct classification (shaded column) and miss classification (the other columns) for ASK, FSK and PSK modulation signals with Th1=2, Th2=0.667, Th3=2, Th4=2, Th5=2 and Th6=-2.

Table (2) Probability of correct and miss classification for ASK signal

(S/N) (dB)	ASK %	FSK %	PSK %	Other %
Without noise	100	0	0	0
20	98.1481	1.8519	0	0
15	88.440	11.560	0	0
10	78.4314	19.6078	1.9608	0
5	72.8814	20.339	5.0847	1.6949
0	53.3333	24.4444	22.2222	0
-5	35.5556	26.6667	33.3333	4.4444

Table (3) Probability of correct and miss classification for FSK signal

(S/N) (dB)	ASK %	FSK %	PSK %	Other %
Without noise	0	100	0	0
20	2.0833	97.9167	0	0
15	14.5455	85.4545	0	0
10	22.9167	77.0833	0	0
5	24.0741	68.5185	5.5556	1.8519
0	30.3571	50	16.0714	3.5714
-5	24.4898	20.4082	48.9796	6.1224

Table (4) Probability of correct and miss classification for PSK signal

(S/N) (dB)	ASK %	FSK %	PSK %	Other %
Without noise	0	0	100	0
20	3.5088	0	96.4912	0
15	14.5455	0	85.4545	0
10	22.449	2.0408	75.5102	0
5	30.7692	3.8462	65.3846	0
0	26.5306	14.2857	53.0612	6.1224
-5	27.5	35	32.5	5

From the above tables, it seems that, the probability of correct classification is affected by AWGN and there is a misclassification at 0dB signal to noise ratio.

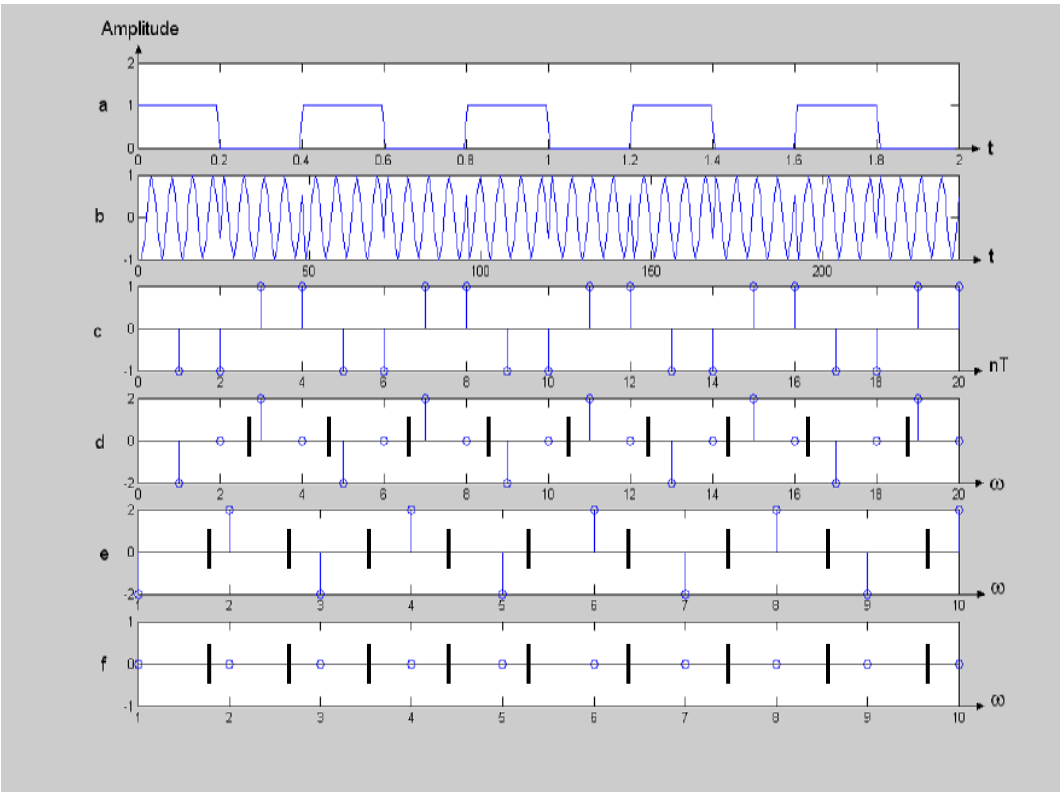

Fig. (5): 2 samples/bit PSK signal analysis

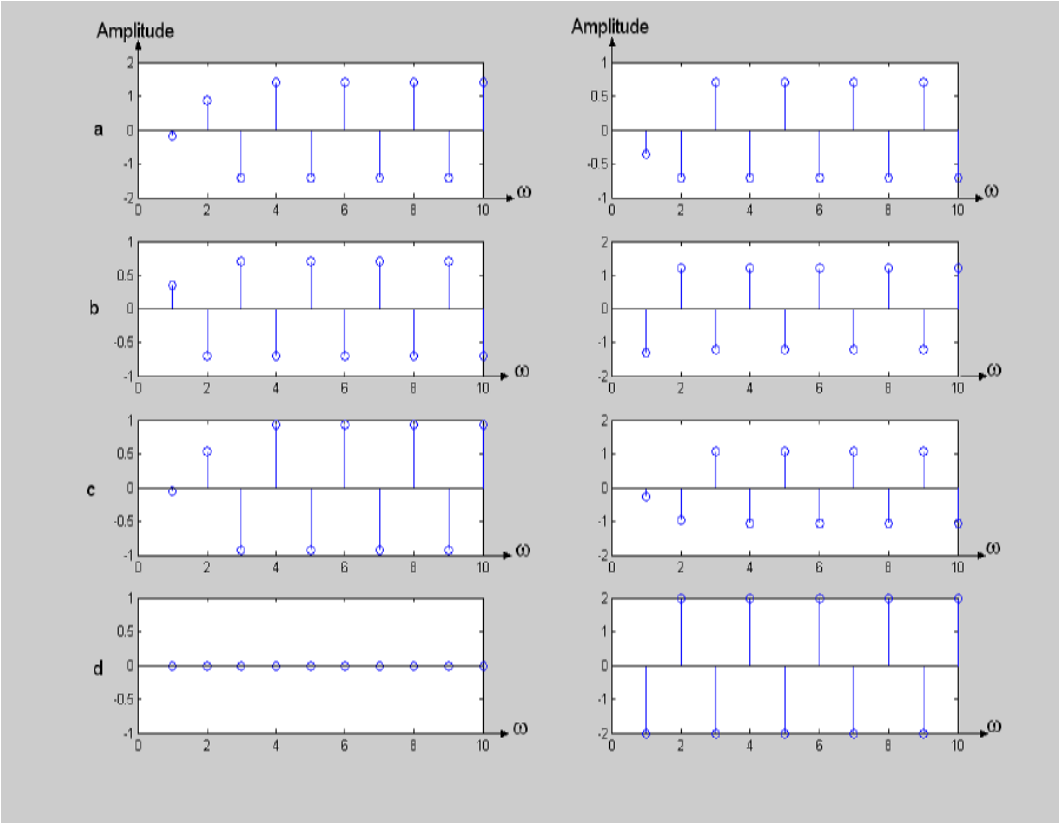

Fig. (6): Two samples PSK signal analysis using different types of wavelet functions a. HP and LP Coif1 wavelet output, b. HP and LP db2 wavelet output, and c. HP and LP bior2.2 wavelet output

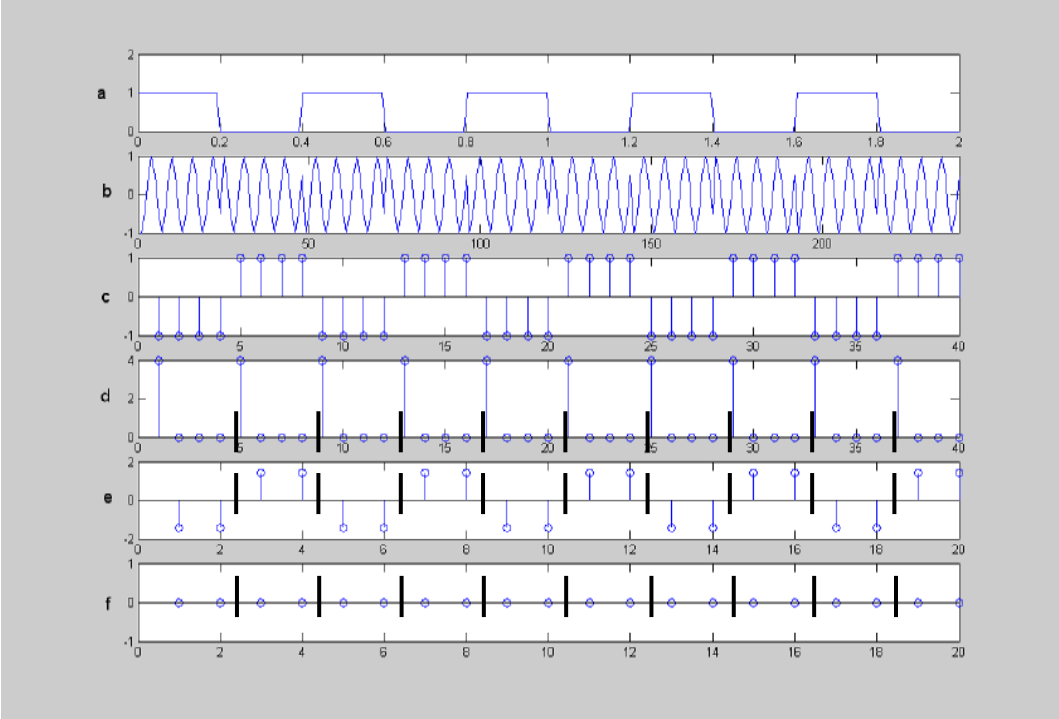

Fig. (7): 4 samples/bit PSK signal analysis a. Binary digital pulses. b. PSK waveform. c. Samples of PSK signal. d. FFT output. Low pass wavelet filter output (first level). f. High pass wavelet filter output (first level)

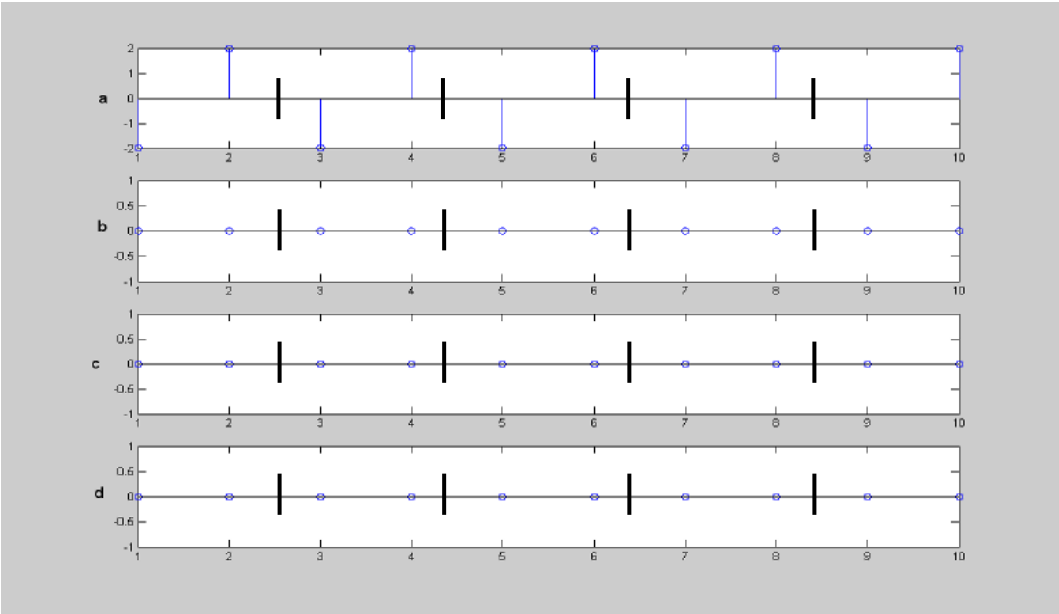

Fig. (8): 4 samples/bit PSK signal analysis (second level)

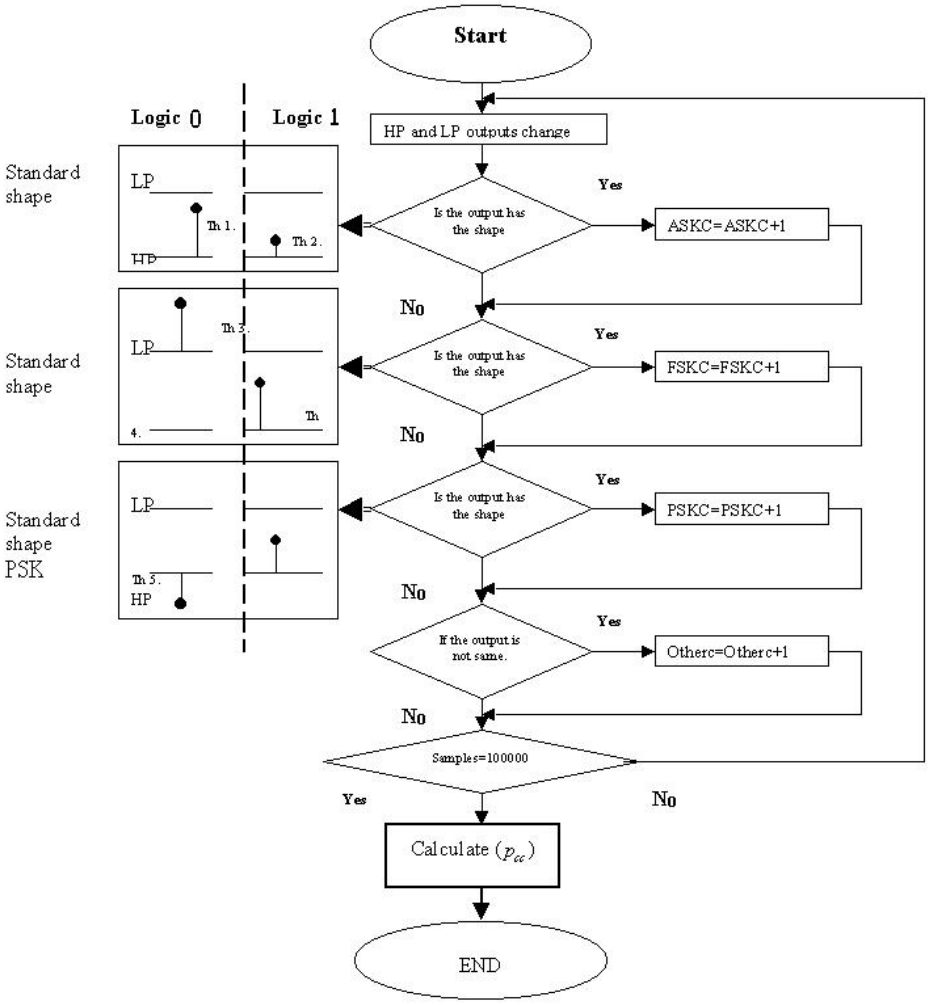

Fig. (9): Flow chart of decision algorithm

4. Conclusions

The complexity of the FFT algorithm used for signal classification limits the effectiveness of such system especially at high bit rate. In the current work, a wavelet filter algorithm is used instead of the FFT algorithm. The two algorithms are tested using computer simulation. As a result one can point out the following:

a. The complexity of the wavelet algorithm is less than that for FFT algorithm. This reduces the time required to complete the classification. For example, for 4samples/bit, the time required for the wavelet algorithm is nearly one fourth of that of the FFT algorithm.

b. The result of different tests and the mathematical proof show that the Haar function is the most suitable function for classification of binary digital signals. Moreover, the Haar function is less in complexity for classifier implementation due to its nature (simplicity).

c. The probability of miss-classification of the wavelet algorithm is increased with the reduction of the signal to noise ratio and the classifier is failed to classify different types of modulated signals at nearly 0dB signal to noise ratio.

References

[1] J.G. Proakis, "**Digital Communications**", McGraw-Hill Series in Electrical and Computer Engineering (2001).

[2] A.J.K. Hummady, "Classification of Digital Modulation Using Wavelet Transform", M.Sc. Thesis, University of Technology (Iraq), September (2004).

[3] A. Graps, "**An Introduction to Wavelets**", *private communications* (1995).

[4] H.K. Chaiel, "Design and Implementation of Branch Hopped Wavelet Packet System", Ph.D. Thesis, Al-Rasheed College for Engineering and Science (Iraq), January 2003.

[5] W. Sweldens, *Proc. IEEE*, 184(4) (1996) 680.

[6] L. Hong and K.C. Ho. "Identification of digital modulation types using the wavelets transforms" Academic Report, Department of Electrical Engineering, University of Missouri-Columbia, Columbia (USA) 1999.

[7] P. Lallo, "Signal classification by discrete Fourier transforms", *private communications* (1999).

[8] T.K. Moon and W.C. Stirling, "**Mathematical Methods and Algorithms for Signal Processing**", Prentice-Hall Inc. (New Jersey) (2000).

This article was reviwed by the Scientific Experience of Meridex Corporation, CANADA, and the Department of Electronic and Communications Engineering, Faculty of Engineering, Al-Nahrain University, IRAQ

WORKSHOPS

The 5th International Workshop on Adaptive Optics for Industry and Medicine
29 August - 2 September 2005
Beijing, China
SPIE is a cooperating organization and will publish proceedings

SYMPOSIA

SPIE Europe International Symposium on Remote Sensing
19 - 22 September 2005
Bruges, Belgium
Abstracts Due 21 March 2005
Exhibition

25th SPIE International Symposium Photomask Technology
3 - 7 October 2005
Monterey, California USA
Abstracts Due 18 April 2005
Exhibition

The Fourth International Symposium on
Multispectral Image Processing and Pattern Recognition (MIPPR)
31 October - 2 November 2005
Wuhan, China
SPIE is a Technical Cosponsor and will publish the proceedings.

International Symposium APOC 2005
Asia-Pacific Optical Communications
6 - 10 November 2005
Shanghai, China
Abstracts Due 9 May 2005

Annabelle C. de Grave*
George L. Manterčk

Department of Solid State Sciences,
Gent University, Krijgslaan 281 S1,
B-9000 Gent, Belgium
Email: annabelledegrave@gent.be

Annealing Effect on the Photoluminescence of CdTe/CdSe Thin Film Photovoltaic Devices

The depth dependence of photoluminescence from as grown and $CdCl_2$ treated polycrystalline CdSe/CdTe solar cells has been compared using a bevel etch technique. It has been found that the three emission bands observed at 1.59eV, 1.55eV and 1.45eV all became more intense after the treatment, with the emission at 1.55eV near the CdSe/CdTe interface being the most affected.

Keywords: *Thin films, CdTe solar cells, CdSe-based devices, photoluminescence*

Received: 13 April 2005, Revised: 18 June 2005, Accepted: 20 June 2005

1. Introduction

There is a great deal of interest in the production of a large area low cost thin film photovoltaic device with efficiency great enough to allow commercial development. One of the most promising contenders for this is the CdTe/CdSe material system. These layers can be grown by the low cost close space sublimation (CSS) technique, which produces polycrystalline structures. Theoretical calculations indicate this material system may have conversion efficiency greater than 29% [1-4].

Post growth treatment is known to affect the cell by increasing the grain size, converting the material from p-type to n-type [5], increasing the heterojunction uniformity [6] and changing the current transport mechanism from tunnelling to thermally activated [7]. As a result, the open-circuit voltage (V_{OC}), short circuit current density (J_{SC}) and fill-factor all increase for the cell while the series resistance (R_S) decreases.

Photoluminescence (PL) is a useful tool for the analysis of these samples since it is in principle capable of detecting energy levels resulting from the $CdCl_2$ treatment, the annealing, extended defects or out-diffusion from the substrate. Also, the relative intensity of PL lines can give an indication to the extent to which non-radiative recombination is important in a given sample. In this study the PL technique has been combined with bevel etching, which has enabled depth dependent information to be obtained from the CdTe layer.

2. Experimental Details

The two devices studied were made in the same run and consist of 6μm of polycrystalline CdTe on a thin (100nm) layer of CdSe, both layers being deposited by close space sublimation (CSS) onto ITO coated glass. Half of the sample was then coated with $CdCl_2$ and annealed in air for 30 minutes at 400°C. Bevel etching was achieved by slow immersion into a bromine, methanol and ethylene glycol etchant through a liquid methanol/etchant interface. The bevel etch gave a varying thickness of CdTe on the CdSe layer. The depth profile of the CdTe along the device was measured using an Alpha Step 200. The structures were placed in a closed cycle helium cryostat mounted on a translation stage and the PL measured at 10K.

3. Results and Discussion

Three luminescence bands were observed in both samples as shown in figure 1. The one at 1.59eV results from donor or acceptor bound excitons. The 1.55eV band has been variously ascribed to either oxygen O_{Te} acceptors [8] or cadmium vacancy V_{Cd} complex based acceptors [9] participating in a donor-acceptor pair (DAP) recombination. A further band at 1.45eV is characteristic of a further complex DAP emission often seen in CdTe. There were some important differences between the spectra of the two samples. The $CdCl_2$ treatment causes a general increase in luminescent intensity indicating either an increase in the concentration of the active centers or a decrease in the non-radiative

recombination sites. The latter is certainly important since the treatment is known to suppress recombination in the device and is associated with grain growth and a reduction in dislocation stacking fault density [10].

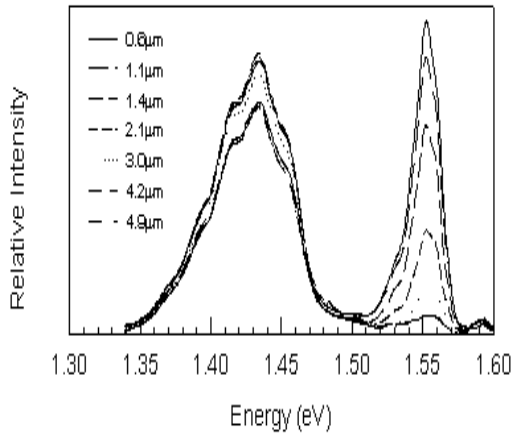

Fig. (1): PL spectra of $CdCl_2$ treated sample from the CdTe layer at different depths from the junction

Bevel etching has enabled the depth dependence of the luminescence to be investigated as shown in figures 2 and 3. For both the as grown and $CdCl_2$ treated samples the 1.44eV band is most intense in the bulk of the layer with the broad maximum being slightly nearer the interface for the $CdCl_2$ treated sample. The origin of the DAP luminescence is known to be complicated and possible assignments such as (V_{Cd}-Cl_{Te}) as the acceptor and Cl_T as the donor are speculative.

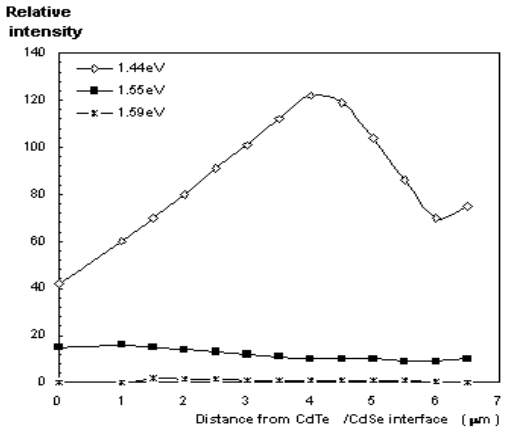

Fig. (2): Variation of emission intensities with the distance from CdTe/CdSe interface for as grown sample

We can only state that there is likely to be some variation in the concentration of active centers throughout the layers both before and after treatment. The excitonic luminescence is uniform in both samples. If the acceptor bound excitonic luminescence is related to acceptors responsible for p-type conductivity at room temperature then it must be remarked that the surface application of $CdCl_2$ and air bake have been remarkably effective in producing homogenous doping in the polycrystalline material.

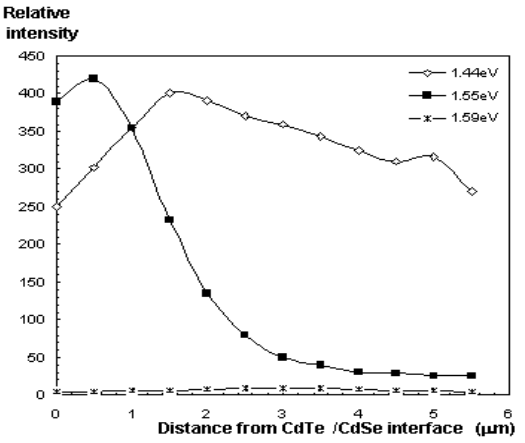

Fig. (3): Variation in emission intensities with the distance from CdTe/CdSe interface for $CdCl_2$ treated sample

The greatest variation in the spatial distribution of luminescence was seen for the 1.55eV peak which was changed by the $CdCl_2$ treatment from being weak and uniform in the as grown sample (figure 2) to being strong in the half of the film nearest the substrate (figure 3). Given the history of the sample the more likely of the two reported assignments in this case is V_{Cd} complexes rather than O_{Te}. This is further implicated by the supposition that if both added Cd and displaced Te are substitutional and Cl incorporates as Cl_{Te} then addition of each unit of $CdCl_2$ creates one cadmium vacancy in some form. However a contribution from the substrate possibly through Na, In, S or Sn out diffusion cannot be ruled out.

4. Conclusion

A PL/bevel etching technique has been shown to be valid for use in comparing the spatial distribution of luminescence throughout the thickness of the CdTe layer in these structures. The general enhancement of the luminescence by the treatment is thought to be associated with grain boundary passivation, which reduces competition with radiative routes. The large increase in the 1.55eV emission is interpreted as resulting from an increase in DAP emission involving V_{Cd} sites present forming complexes with Cl atoms on adjacent Te sites. Considering the large increase in the intensity of this emission, it would seem that it is important in the understanding of the increase in device efficiency.

Acknowledgements

We would like to thank D. Bonnet and H. Richter, ANTEC GmbH, Germany, for the provision of the samples, A. Crozier for her project work on the etching and EPSRC for the funding of some of the work in this project. JME gratefully acknowledges funding through an EPSRC studentship.

References

[1] A.W. Brinkman, "Properties of Narrow Gap Cadmium-Based Compounds", ed. P. Capper, *Electronic Materials Information Services*, No.10. IEE (London) (1994) 591.
[2] J. Versluys, P. Clauws, P. Nollet, S. Degrave and M. Burgelman, *Thin Solid Films*, 431-432 (2003) 148.
[3] P. Nollet, M. Kontges, M. Burgelman , S. Degrave, R. Reineke-Koch, *Thin Solid Films*, 431-432 (2003) 414.
[4] S. W. Townsend, T. R. Ohno, V. Kaydanov, A. S. Gilmore, J. D. Beach, and R. T. Collins, Influence of Stressing at Different Biases on the Electrical and Optical Properties of CdSe/CdTe Solar Cells, *private communications (2002)*.
[5] S. Seto, A. Tanaka, Y. Masa and M. Kawashima, *J. Cryst. Growth,* 117 (1992) 271.
[6] S.A. Galloway, A.W. Brinkman, K. Durose, P.R. Wilshaw and A.J. Holland, *Appl. Phys. Lett.*, 68 (1996) 3725.
[7] H.M. Al-Allak, S. Galloway, A. Brinkman, K. Durose, H. Richter and H. Bonnett, Proceedings of the 13th European Photovoltaic Solar Energy Conference, Nice, 23-27 October, 2 (1995) 2135.
[8] K. Akimoto, H. Okuyama, M. Ikeda and Y. Mori, *Appl. Phys. Lett.*, 60 (1992) 91.
[9] J.M. Figueroa, F. Sanchezsinencio, J.G. Mendozaalvarez, O. Zelaya, C. Vazquezlopez and J.S. Helman, *J. Appl. Phys.*, 60 (1986) 452.
[10] Y. Loginov, K. Durose, H.M. Al-Allak, S. Galloway, S. Oktik, A. Brinkman, H. Richter and D. Bonnet, *J. Cryst. Growth.*, 161 (1996) 159.

This article was reviwed at Physics Science and Research Center, Ministry of Science and Technology, Baghdad, IRAQ, and School of Applied Sciences, University of Technology, Baghdad, IRAQ

CONFERENCES

10th OptoElectronics and Communications Conference (OECC 2005)
5 - 8 July 2005 Seoul, South Korea
SPIE is a technical cosponsor

Visual Communications and Image Processing (VCIP 2005)
12 - 15 July 2005 Beijing, China
SPIE is a cooperating organization

ICOXX-20th Congress of the International Commission for Optics
21 - 26 August 2005 Changchun, China
SPIE is a cosponsor

CONFERENCES

International Congress on Optics and Optoelectronics
28 August - 2 September 2005 Warsaw, Poland
Sponsored by SPIE Europe and SPIE Polish Chapter (Exhibition)
Abstracts Due 14 February 2005

4th Pacific Rim Conference on Photonics and Imaging in Biology and Medicine (PIBM 2005)
3 - 6 September 2005 Tianjin, China
SPIE is a cooperating organization and will publish proceedings

Seventh International Conference on Correlation Optics
6 - 9 September 2005 Chernivtsi, Ukraine
Sponsored by SPIE Ukraine Chapter and SPIE Russia Chapter.
SPIE will publish proceedings.

Photonics North 2005
12 - 14 September 2005 Toronto, Canada
Cosponsored by SPIE and Canadian Photonics Consortium.
Abstracts Due 28 March 2005 (Exhibition)

Atomic and Molecular Pulsed Lasers
12 - 16 September 2005 Tomsk, Russia
Sponsored by SPIE Russia Chapter.

PECS 2005: Photon Echo and Coherent Spectroscopy
18 - 25 September 2005 Kaliningrad, Russia

New High Angular Resolution Detection System for Direction Recognition

Husam H. Habib[1]
Walid K. Hamoudi[2]
Raid A.W. Ismail[3]

(1) Aeronautics and Space Research Center, Ministry of Science and Technology, Baghdad, IRAQ
h_hanna@coolgoos.com
(2) School of Applied Sciences, University of Technology, Baghdad, IRAQ
(3) Physics Science and Research Center, Ministry of Science and Technology, Baghdad, IRAQ

A digital angular resolution detection device using linear detector arrays has been designed and fabricated in two models; with accuracy better than (±1°) and (±2°) respectively. The principle of operation is based on encoding the radiation angle of arrival by using a code mask based on random fractal generation.

Keywords: Angular resolution, Direction recognition, Position sensitive device, Multichannel detector, Resolution

Received: 13 Feruary 2005, Revised: 3 July 2005, Accepted: 20 June 2005

1. Introduction

To compute the displacements of the light spots, a position detector capable of dealing with multiple spots must be used. One solution is to use an imager (CCD, Vidicon), so that an image frame is grabbed and special data-reduction algorithm reduces the bitmap into coordinate information and this, however, requires considerable processing time [1-2].

Scanning angle trackers also used to localize the angular position using a detector (single or matrix) [3], and uses some technique (mechanical, electrical) to change the angle at which the detector is pointed (or to steer the laser beam [4]). By monitoring both the signal output and the encoder's angle output, one could identify the angular position of the radiation source as the mirror "scans" the image across the detector. While the concept of scanning systems is simple, the complexity of such a system is enormous [5-6].

On the other hand, there are several different layouts of non-imager position sensitive detector (PSD) [7]. The most popular is LEP (Lateral Effect Photodiode) "a segment of photodetective silicon with either two or four terminals for signal output" and QD (Quadrant Detector) "four photodiodes with common substrate, which are electrically isolated from each other". The main advantage of using a PSD is that the information on the spot centroid position are readily available after extremely simple mathematical calculations on its output signals,

$$x_{LEP} = \frac{I_A - I_C}{I_A + I_C}$$

and

$$x_{QD} = \frac{(I_A + I_B) - (I_C + I_D)}{I_A + I_B + I_C + I_D}$$

for x-direction (Fig. (1)), which overcomes the image processing and increases operational speed. An A/D converter must be used in the electric circuit to deal with the PSD output signals [2].

Fig. (1): QD and LEP operation principle [2]

In the present work, a new design of an angular resolution device, based on employing a one-dimensional detector array is presented. In this system, whether each of the array elements is illuminated or not it depends on the incidence angle of the laser beam at the device. The illuminated element will be considered as logic

"1" otherwise "0", that can be done by placing a code mask designed by random fractal generation in front of the array causing different combinations for different angles of arrival. One additional detector element or more is employed as a reference to other elements of the array to form a reference channel. This reference channel is required in the device in order to establish signal levels for deciding whether a signal is a "1" or a "0". The reference channel designed to be illuminated over the full field of view of the device. Low price, compactness and simplicity are the important characteristics of the electric circuit that was built. The signal obtained from the device is already digitally coded and all we need is a one-stage comparator amplifier, which compares the signal received from a specific detector element with the signal from the reference detector element. We will describe two different models of angular resolution device that had been designed, which rely on the same principle:

2. Experimental Work

2.1 Model One Specifications

This model is designed by constructing adjacent channels, which are optically isolated from each other. Their number is equal to the detector array elements. The code mask is positioned at the top of the channels while the detector array is located at the bottom as seen in Fig. (2), which shows four basic components:

1) Code mask, (made from transparent material) having an appropriate number of channels, in which the rows are arranged in different code configurations.

2) Channel's body with high reflecting partitions acts like a guide system, and optical isolation is maintained between the signals in the adjacent channels.

3) Slot mask, (made from an opaque material) which works with the code mask to define the incidence angle of the incoming light.

4) Linear detector array having a number of elements that matches the number of the constructed channels and the code mask as well.

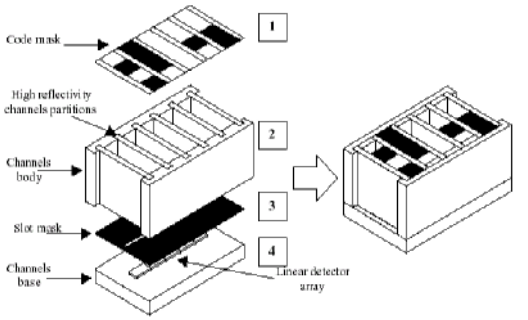

Fig. (2): Model One Head (Assembly Isometric View)

When the laser beam illuminates the device at a certain angle, the code mask shadow will project its image on the detector array plane. Here, we need to add another mask exactly above the detector array, which contains a slot to clip the code mask shadow in a suitable width before illuminating the detector elements. For incidence angles exceeding (±45°), the shadow will be lengthened causing an error in the angle measurement. A limit for the field of view of (90°) is maintained by determining the channels height, which is equal to the distance between the code mask and the slot. This limitation could be overcome by more complex design of the code mask. If the device is positioned to measure the angular resolution in the azimuth direction, then the ideal case is when the component of the optical signal is zero in the elevation direction. In this case, the reflecting partitions bounding the optical channel may have minimal function. Practically, the laser source position could contain optical components in both axes. The reflecting partitions at the sides of the optical channel are important, not only to prevent the laser from illuminating adjacent detector elements, but to ensure that laser light reaching the detector element has minimal loss after several reflections. For this reason, the partition between channels was made of high reflecting surface acting like a waveguide, (see Fig. (3)), to insure that the image of the shadow will fall on the slot plane as well. Narrowing the channels more and hence increasing their number improve the resolution.

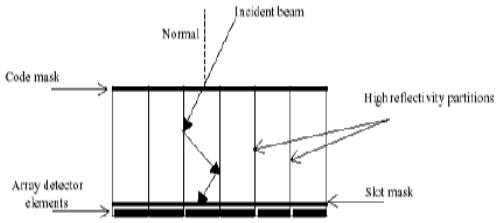

Fig. (3): Model One (Front View)

It is obvious from the above design that the device can measure the angle of the arriving signal in one direction only "azimuth" (for example) at a time, therefore, another similar device oriented (90°) is needed to measure the angle of arrival of the same laser source in the "elevation" direction.

2.2 Model Two Specifications

Model Two is designed (same as Model One) by constructing adjacent channels, optically isolated from each other with a number equal to the detector array elements. The major difference from Model One is that the channel's partition here is perforate in a semicircular shape so that the code mask can be fixed in a hemicylindrical

form, (see Fig. (4)), by placing a cylindrical lens at a distance equal to the focal length (this can be managed by two bushes at each end of the lens). The basic operation of Model Two is illustrated in Fig. (5). As the figure shows, the incident collimated laser beam is focused by the cylindrical lens as a line, then passes through the hemicylindrical code mask to illuminate the chambers (channels) that contain the detector array elements located below. Elements of the detector array are either illuminated "1" or dark "0", depending on the channel and the angle of incidence of light passing through the code mask. The detectors illumination in this model depends on the multi reflections that take place in the chambers, (while in Model One, the detector depends on direct illumination), so that it is very important here to make the walls of the chambers of high reflectivity. The main advantage of this model is that almost (180°) field of view, which is twice of that achieved from the first model, can be detected.

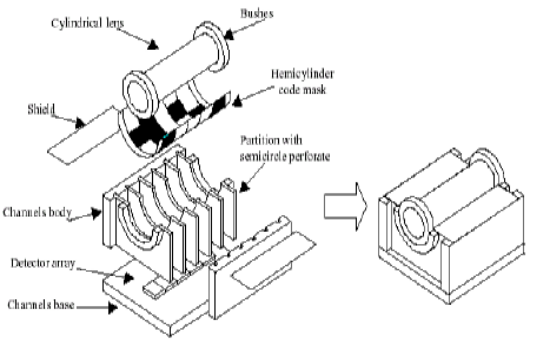

Fig. (4): Model Two Head (Assembly Isometric View)

As in Model One, the coding in Model Two operates in only one axis at a time, so that a second similar device would be required to obtain angular resolution in the other axis.

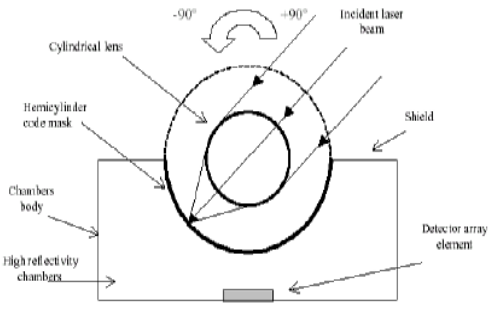

Fig.(5): Model Two (Side View)

2.3 Mask Designing and Making

Computer software, based on random fractal generation [8], was written to create the mask design. The larger the channel number (bits number), the higher resolution angular analysis we may get, but the more complex the mask pattern will result. The mask will look like a series of small windows of various lengths in order to generate a digital code. As a result the code can limit the variation of the angle to 1 bit at a time for any change in the angle of arrival of the incoming light. As a function of the angle of arrival, the linear array of the detector illumination through the mask will change, thus producing different codes for the various angular positions of the beam. The mask is made from a high transparent sheet and the pattern was stamped on it with the highest accuracy that could be achieved. The pattern consists of adjacent channels, each of which contains transparent or opaque zones, so that every row across the channels will give different code of "0's" and "1's".

2.4 Angular Measurements Setup

In order to measure different angles of arrival, a platform needed to be designed and manufactured to fasten the device, capable of rotating with fine-tuning instead of rotating the laser source around the device up to (±90°). In order to measure the angle of arrival, the rotating table was supplied by a protractor. The collimated beam will fall on a mirror at (45°), as shown in Fig. (6), so as eventually fall vertically on the measurement platform.

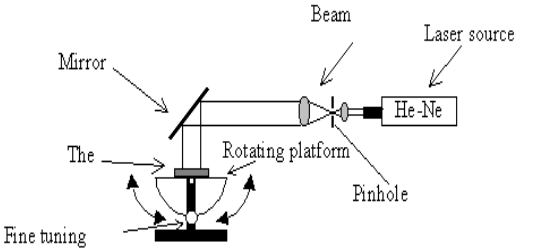

Fig.(6): Measurement setup arrangement.

3. Results and Discussions

3.1 Mask Resolution

From the device description and its operation principles, the mask is considered as the major item that determines its characteristic. More than one design was attempted with different resolution capabilities. In the present work, one type is reviewed in order to prove the idea of achieving fairly good resolution with a relatively easy manufacturing. The mask has 48 discrete intervals each of them has a different code, (see Fig. (7)). These codes are a combination of 6 channels (bits number). The angular measurement resolution can be determined by dividing the field of view on the number of intervals. For Model One, the angular resolution is about (±0.9°) and its field of view (90°) divided into 48 discrete angular intervals, each

interval is (1.8°). The (180°) field of view of Model Two will be divided into intervals of (3.6°) giving an angular resolution of (±1.8°). The same mask's design is used for both models, but with different dimensions. To simplify the design the mask contains only one reference channel at the middle of the other channels.

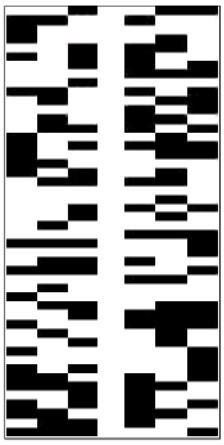

Fig.(7): The mask design

3.2 Device Characterization Tests

The device was characterized using a collimated laser beam whose irradiance direction was monitored at the device head. The angular coverage (field of view) of each model and the angular accuracy were determined. Each head of the two models was mounted on the rotating table platform in away so that the beam is normal to the planner element array, thus, the setup insures that the device is maintained continually in the beam for all the discrete angular positions measured.

3.2.1 Threshold Level Determination

To evaluate the performance of the comparison process between the reference channel signal and other channels output, the outputs signal from the electric circuit can be controlled in order to fix the optimum value of the reference signal to establish signal levels for determining whether the signal in a detector elements is "1" or "0". A normalized signals for the reference channel and one of the channels is plotted in Fig. (8) for a full scan to the field of view (-45° to +45°). From the figure, we can notice that the reference signal output is almost constant all over the scanned view with some limited deviation due to a small amount of scattered light at certain angles. The other channel varied according to the incident angle and the mask. The harmony between the code and the slot mask is important to define the number of divisions of the FOV. Thus directly affects the angular analysis accuracy.

3.2.2 Angular Accuracy Determination

After fixing the device head upon the rotating platform, which is supplied by a protractor, the angle of the platform was read relatively to the beam. The angle was changed gradually from (-45° to +45°) for Model One and from (-90° to +90°) for Model Two. Whenever the digital code was changed, the angle was recorded to compare it with real values. To explain this point, Fig. (9) shows the fine tuning of the real angles versus the measured angles.

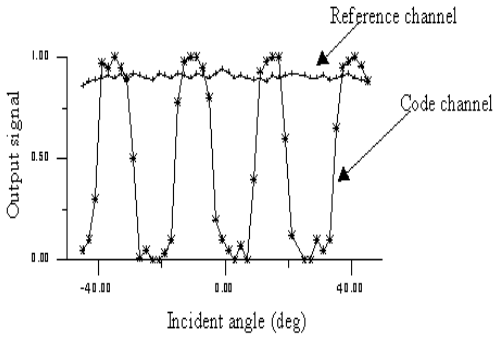

Fig.(8): A normalized signals comparison

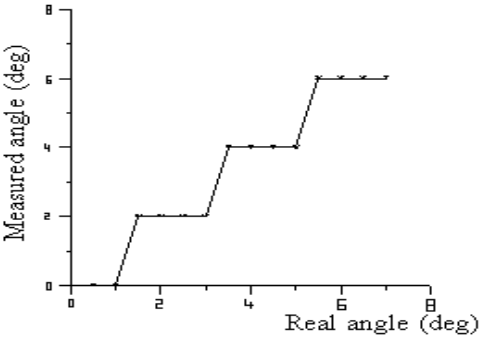

Fig.(9): Fine tuning real angle versus measured angle plot

Fig. (10) shows a plot between the angle of arrival as recorded on the device versus the actual angle that can be readout from the protractor. The linear relationship shows an identity between the measured and true angle of arrival. Fig. (10a) shows a good agreement between the two angles for Model One case while Fig. (10b) shows that Model Two has some sort of nonlinearity originated from missreading of some codes or bits at the corner zones. This result is expected since the body configuration of the head device has a rectangular cross-section. All these measurements were taken at elevation angle equal to zero. By varying the laser irradiance incident on the device head, it was established that the device was capable of identifying the angle of arrival of the laser beam with relatively

high angular resolution about (±0.9°) for Model One and (±1.8°) for Model Two.

3.2.3 Effect of Elevation Deviation

Another test, which took our attention, was to see how much the device can hold and keep functioning correctly when elevation angle is changed (more than 0°) during azimuth angle measurement. Model One shows good accuracy results for the measurement at a number of elevation angles between (-45°) and (+45°). The measured values of the angles, and the deviation from the calculated values are recorded for each of the elevation angles. We note from the measurements that there is an accuracy for this model of about (±0.9°). If this deviation is taken into consideration, then it is seen that most of the angles are correct within the elevation angle from zero up to (±15°), between (15°-30°) misbits occurred. At elevation angles more than (30°) for both sides, the error is greater. At maximum elevation angle (±45°) the angular error was noted to be above (2°).

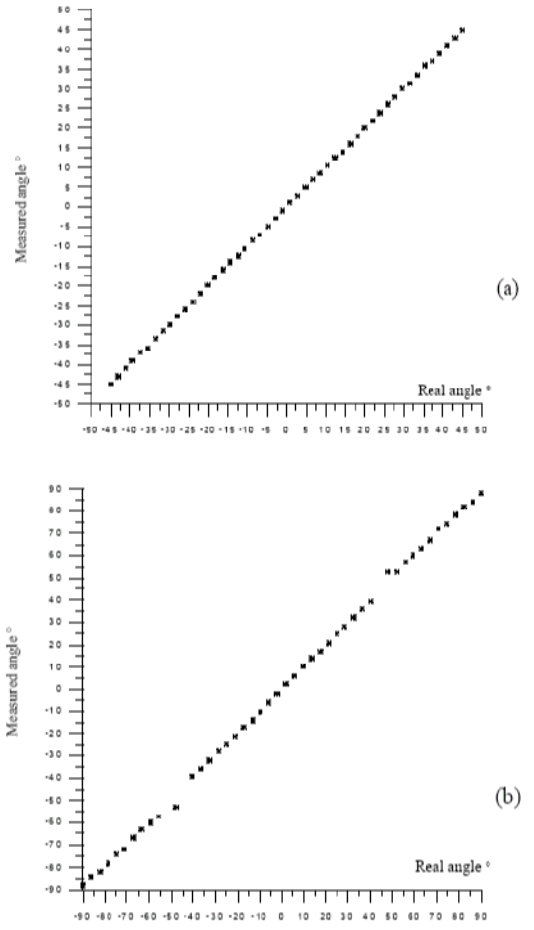

Fig.(10): The relationship between the measured versus real angle of arrival. (a) Model One (b) Model Two

At low elevation angle the reflecting partitions function efficiently but with more angle increase, some losses will take place because of the multiple reflections inside the channel. A higher accuracy can be achieved if the reflectivity of the partition is made as high as possible. We can state that Model One device provides a (±45°) azimuth by (±45°) elevation field of view with optimum case when azimuth angle equal to zero. Model Two shows acceptable accuracy results at a number of elevation angles. The measured values of the angles, and the deviation from the calculated values are recorded for each of the elevation angles.

Model Two provides a (±90°) azimuth field of view by a relatively limited elevation angle. The optimum case is when azimuth angle equal to zero. The elevation angle deviation causes some deformation in the incident beam image after being focused on the mask by the cylindrical lens. This deformation becomes significant past (±10°) leading to a lower angular resolution. For both models, this problem can be overcome by controlled servo of the platform in order to align the device heads with the beam direction site, and the device will work at the optimum case all the times.

4. Conclusions

Two angular resolution devices, both based on encoding the incident light are designed, constructed and analyzed. The angular resolution has successfully passed the laboratory testing. The results confirm its capability to localize an irradiance source with excellent accuracy. Model One employing shadow technique achieved FOV of (90°) (-45° to +45°) with angular resolution of (±0.9°). Model Two, on the other hand, employs a cylindrical lens with (±1.8°) angular resolution and (180°) FOV (-90° to +90°). Development is underway to increase the angular resolution by larger number of elements (higher bit number).

References

[1] D.W. de Lima Monteiro and G. Vdovin, "CMOS-compatible wavefront detector", Electronic Instrumentation Laboratory, Delft University of Technology, The Netherlands, 2000.

[2] A. Makynen, "Position-sensitive devices and sensor systems for optical tracking and displacement sensing applications", University of Oulu, Finland, 2000.

[3] S. Arnon and N.S. Kopeika, “Adaptive suboptimum detection of an optical pulse-position-modulation signal with a detection matrix and centroid tracking”, *J. Opt. Soc. Am. A*, 15(2) (1998) 443-448.

[4] E. Hallstig, J. Stigwall, M. Lindgren and L. Sjoqvist, “Laser Beam Steering and Tracking using a Liquid Crystal Spatial Light Modulator”, Sweden, 2004.
[5] H. Toshiyoshi, W. Piyawattanametha, C.T. Chan and M.C. Wu, "Linearization and analysis of electrostatically actuated MEMS 2D optical scanner", Presented at Hilton Head 2000 Sensor & Actuator Workshop, June 5-8, 2000.
[6] J.A. Hancock, "Laser intensity-based obstacle detection and tracking", John A. Hancock, January 26, 1999.
[7] N. Massari, M. Gottardi, L. Gonzo and A. Simoni, "High speed digital CMOS 2D optical position sensitive detector", ESSCIRC 2002.
[8] J.-F. Gouyet, **"Physics and Fractal Structures"**, Springer-Verlag, Berlin, 1996, 19-20.

This article was reviwed at Center of Applied Mathematical Sciences, University of Southern California, U.S.A, the Department of Electric and Electronic Engineering, University of Technology, Baghdad, IRAQ

SYMPOSIA
ON OPTICS AND OPTICAL TECHNOLOGY

SPIE Europe International Symposium on Optical Systems Design
12 - 16 September 2005 (Abstracts Due 28 February 2005) Jena, Germany
Exhibition

Boulder Damage Symposium XXXVII
Annual Symposium on Optical Materials for High Power Lasers
19 - 21 September 2005 (Abstracts Due 31 May 2005) Boulder, CO USA
Abstract submissions will be accepted starting in mid February

SPIE Europe Symposium Optics/Photonics for Defence & Security
26 - 29 September 2005 (Abstracts Due 11 April 2005) Bruges, Belgium
Exhibition

The Second International Symposium on Advanced Optical Manufacturing and Testing Technologies (AOMATT)
2 - 5 November 2005 Xian, China
SPIE is a technical cosponsor and will publish the proceedings

IRAQI JOURNAL OF APPLIED PHYSICS

" INSTRUCTIONS TO AUTHORS "

A new Iraqi specialized quarterly periodical dedicated to publishing original papers and letters in:

Applied & Nonlinear Optics	Electronic Materials & Devices	Quantum Physics & Spectroscopy
Applied Mechanics & Thermodynamics	Laser Physics & Applications	Semiconductors & Optoelectronics
Digital & Optical Communications	Plasma Physics & Applications	Solid State Physics & Applications

CONTRIBUTIONS

Contributions to be published in this journal should be original research works, i.e., those not already published or submitted for publication elsewhere, individual papers or letters to editor.

SUBMISSION OF MANUSCRIPTS

Manuscripts should be submitted to the editor at the mailing address:

Iraqi Journal of Applied Physics
Managing Editor
P. O. Box 55259, Baghdad 12001, IRAQ
irq_appl_phys@yahoo.com

Iraqi Journal of Applied Physics
Editor-In-Chief
P. O. Box 55159, Baghdad 12001, IRAQ
editor_ijap@yahoo.com

MANUSCRIPTS

Two copies with soft copy on a 3.5" diskette should be submitted to Editor in the following configuration:

- Double-spaced one-side A4 size with 2.5 cm margins of all sides
- 12pt Times New Roman font
- Letters should not exceed 5 pages, papers no more 20 pages and reviews are up to author.
- Manuscripts presented in English only are accepted.
- Authors confirm affiliations, addresses and emails. Email is necessary for correspondences.
- English abstract not exceed 150 words
- 4 keywords (at least) should be maintained on (PACS preferred)
- Author(s) should express all quantities in SI units
- Equations should be written in equation form (italic and symbolic)
- Figures and Tables should be separated from text
- Figures and diagrams can be submitted in colors for assessment and they will be returned to authors after provide printable copies
- Charts should be indicated by the software used for
- Only original or high-resolution scanner photos are accepted
- References are written in titles, full-name authors, names of publications, years, volumes, issues and pages (from-to)

PROOFS

Authors will receive proofs of papers and are requested to return one corrected hard copy with a WORD copy on a 3.5" diskette. New materials inserted in the original text without Editor permission may cause rejection of paper.

COPYRIGHT FORM

Author(s) will be asked to transfer copyrights of the article to the Journal soon after acceptance of it. This will ensure the widest possible dissemination of information.

OFFPRINTS

Authors will receive offprints free of charge and any additional offprints can be ordered.

SUBSCRIPTION AND ORDERS

Annual fees (4 issues per year) of subscription are:

- 36 000 Iraqi dinars for individuals and establishments inside Iraq.
- 50 US$ for individuals and establishments abroad.

Fees are reduced by 25% for **I.S.A.R.E.S.T.** members. Orders of issues can be submitted by contacting the editor-in-chief or editorial secretary to maintain the address of issue delivery and payment way.

THE IRAQI JOURNAL OF APPLIED PHYSICS
EDITORIAL BOARD
P. O. Box 55259, Baghdad 12001, IRAQ
Email: editor_ijap@yahoo.com

COPYRIGHY RELEASE

Iraqi Journal of Applied Physics (IJAP)

We, the undersigned, the author/authors of the article titled

……

……

that is presented to the Iraqi Journal of Applied Physics (IJAP) for publication, declare that we have neither taken part or full text from any published work by others, nor presented or published it elsewhere in any other journal. We also declare transferring copyrights and conduct of this article to the Iraqi Journal of Applied Physics (IJAP) after accepting it for publication.

The authors will keep the following rights:

1. Possession of the article such as patent rights.
2. Free of charge use of the article or part of it in any future work by the authors such as books and lecture notes without referring to the IJAP.
3. Republishing the article for any personal purposes of the authors after taking journal permission.

To be signed by all authors:

Signature:……..date: ……..

Printed name: ……..

Signature:……..date: ……..

Printed name: ……..

Signature:……..date: ……..

Printed name: ……..

Correspondence address:

……

……

Telephone:…….Fax:……..email: …….

Note: Please complete and sign this form and mail it to the below address with your manuscript

The Iraqi Journal of Applied Physics,
P. O. Box 55259, Baghdad 12001, IRAQ
Email: irq_appl_phys@yahoo.com ***or*** editor_ijap@yahoo.com
Mobile: 07901274190